Streaming potential in porous media
2. Theory and application to geothermal systems

A. Revil

CNRS-CEREGE, Department of Geophysics, Aix-en-Provence, France

H. Schwaeger and L. M. Cathles III

Department of Geological Sciences, Global Basin Research Network, Cornell University, Ithaca, New York

P. D. Manhardt

GeoGroup Inc., Ithaca, New York

Abstract. Self-potential electric and magnetic anomalies are increasingly being observed associated with hydrothermal fields, volcanic activity, and subsurface water flow. Until now a formal theoretical basis for predicting streaming potential of porous materials has not been available. We develop here a model giving both the macroscopic constitutive equations and the material properties entering these equations. The material properties, like the streaming potential coupling coefficient, depend on pore fluid salinity, temperature, water and gas saturations, mean grain diameter, and porosity. Some aspects of the model are directly tested with success against laboratory data. The streaming potential increases with temperature, grain size, and gas saturation, and decreases with salinity. At the scale of geological structures the model provides an explanation for the presence of kilometer-scale dipolar self-potential anomalies in geothermal systems and volcanoes. Positive self-potential anomalies are associated with fluid discharge areas, whereas negative self-potential anomalies are associated with fluid recharge areas. Self-potential anomaly maps determined at the surface of active hydrothermal fields appear to be a powerful way of mapping the fluid recharge and discharge areas. In the case of free convection the vorticities of the convection pattern generate a magnetic field. The greater these vorticities, the greater the associated magnetic field. It follows that hydrothermal systems act as natural geobatteries because of the flow of pore fluids in the subsurface of these systems.

1. Introduction

There are now many observations of self-potential anomalies associated with the activity of hydrothermal fields and volcanoes [e.g., *Fitterman and Corwin*, 1982; *Sill*, 1983; *Ishido et al.*, 1983; *Massenet and Pham*, 1985; *Antraygues and Aubert*, 1993; *Zlotnicki and Le Mouël*, 1990; *Hashimoto and Tanaka*, 1995; *Sasai et al.*, 1997; *Apostopoulos et al.*, 1997; *Michel and Zlotnicki*, 1998]. These electrical potential anomalies can have large amplitudes (e.g., +2.3 V measured over the Kilauea geothermal area in Hawaii by *Zablocki* [1976], + 2 V measured over the La Fournaise volcano, Réunion Island, Indian Ocean, by *Michel and Zlotnicki* [1998], and +1.0 V measured around the lava dome on Unzen Volcano, Japan, by *Hashimoto and Tanaka* [1995]). Very often, they show dipolar characteristics. Examples include -600/+400 mV in the Long Valley geothermal area in California [*Anderson and Johnson*, 1976], ± 80 mV in the Cerro Prieto geothermal field in Baja California, Mexico [*Fitterman and Corwin*, 1982], -40/+20 mV at Red Hill Hot Spring, Utah [*Sill*, 1983], -200/+100 mV in Ergani, Turkey [*Abdelrahman and Sharafeldin*, 1997], -30/+70 mV at Lesvos Island, Greece [*Apostopoulos et al.*, 1997], and -500/+300 mV on Karthala volcano, Grande Comore, Indian Ocean [*Lénat et al.*, 1998]. Sometimes, the evolution of these electrical potential anomalies is observed with time. For example, *Hashimoto and Tanaka* [1995] observed the development of a bipolar self-potential anomaly with time at the Unzen Volcano on the Shimabara peninsula of southwest Japan. They detected a positive self-potential anomaly in the vicinity of a lava dome and the development of negative self-potential anomalies to its side. In this case these self-potential anomalies was probably the result of an electrokinetic phenomenon related to the local hydrothermal system associated with the cooling process of intruded magma close to the summit of the volcano. *Sasai et al.* [1997] have also observed a positive self-potential anomaly up to +700 mV centered on the summit of Miyakejima Island, a volcano located 150 km south of Tokyo in the Izu-Bonin Arc. This positive self-potential anomaly is surrounded by negative anomalies amounting to -250 mV on the north and -100 mV on the southwestern mountainside. *Anderson and Johnson* [1976], *Ishido and Mizutani* [1981], *Massenet and Pham* [1985], and *Morgan et al.* [1989], among others, have suggested that the self-potential anomalies in geothermal areas and volcanoes could be explained best as the result of electrokinetic effects related to fluid flow. However, no formal theory of these effects has been described in the past. The purpose of this paper is to provide such a theory.

In order to understand and to model the electric and the magnetic fields of electrokinetic nature generated in geothermal environments, four kinds of equations have to be established. They are (1) the constitutive macroscopic relationships between the fluxes (the electrical current density and the hydraulic flux) and the generalized thermodynamic forces, (2) the conservation equations for the fluid mass and the electrical charge, (3) the boundary conditions, which close the system of equations, and (4) the relationships between the material properties of a porous representative elementary volume, the thermodynamic conditions existing in that system (e.g., pore fluid temperature, pH, and ionic strength), and the microstructure of this porous material. These equations are described in this paper, and we discuss, in section 4, some of the implications for geothermal systems and volcanoes of electrokinetic phenomena related to fluid flow, including the effect of free convection.

2. Macroscopic Relationships

We consider a porous material to be composed of an interconnected pore space saturated by a multicomponent electrolyte, and an electrically insulating mineral phase called the matrix (Figure 1). The matrix is composed of mineral grains and the nonconnected porosity. We assume a bimodal grain size distribution with the clay particles representing the small grains. The fine and coarse grain size distributions are assumed to be relatively narrow, and they do not overlap. The term "macroscopic" refers to a representative elementary volume (REV), assuming implicitly that the scale adopted to describe such a volume exists. We use throughout this paper the two following assumptions: (1) The fluid flow inside the interconnected pore space is laminar, and (2) the thickness of the electrical diffuse layer associated with mineral surface charge (Figure 1) is much smaller than the radii of curvature of the interface between the matrix and the interconnected pore space; it is also much smaller than the aperture of throats controlling transport properties in the interconnected pore space (the "flat and thin electrical double layer assumption"). This last assumption is usually valid because the thickness of the electrical double layer is directly related to the salinity of the pore water fluid. In natural conditions found in most geological systems, the salinity is higher than 10^{-3} mol L^{-1}, and the electrical double layer thickness is smaller than 10 nm. Consequently, assumption 2 holds for grain sizes of the order of 0.1 μm or bigger.

2.1. Electric Potential Distribution

Under the previous assumptions the macroscopic constitutive and conservation equations describing the macroscopic electrical current density $\mathbf{j}$ (in A) and the water flux $\mathbf{u}$ (in m s^{-1}) (also called the Darcy velocity) due to the generalized forces applied to the porous medium are

$$\mathbf{j} = \ell_{11}\,\mathbf{E} - \ell_{12}\,\left(\nabla p - \rho_f \mathbf{g}\right), \tag{1}$$

$$\mathbf{u} = \ell_{21}\cdot\mathbf{E} - \ell_{22}\cdot\left(\nabla p - \rho_f \mathbf{g}\right), \tag{2}$$

$$\nabla\cdot\mathbf{j} = -\frac{\partial}{\partial t}[\rho(\mathbf{r},t)], \tag{3}$$

$$\nabla\cdot\mathbf{q} = -\frac{\partial}{\partial t}\left(\rho_f\phi\right), \tag{4}$$

where $\mathbf{q} = \rho_f\mathbf{u}$ is the water mass flux (in kg s^{-1} m^{-2}), ℓ_{ij} $(i \neq j)$ (in m^2 V^{-1} s^{-1}) represents the coupling between the electric and
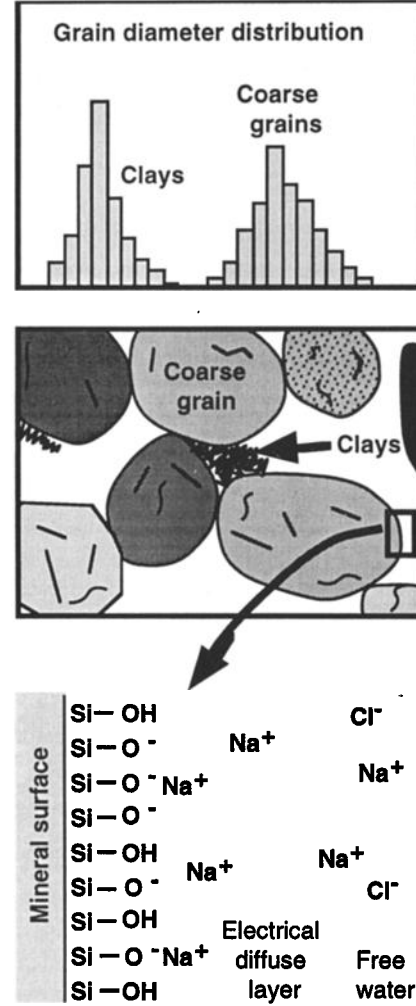

Figure 1. We consider porous materials with a bimodal grain size distribution, the finest grains corresponding to the clay particles. The fine and coarse grains are coated by an electrical double layer with an excess of ions in the vicinity of the mineral water interface. The drag of this excess of ions by the pore water flow is responsible of a macroscopic polarization phenomenon, which leads to the presence of both macroscopic electrical and magnetic fields.

hydraulic forces (with $\ell_{12} = \ell_{21}$ by virtue of Onsager's irreversible thermodynamic theorem [e.g., *Bear*, 1988, p. 87]), p is the pore fluid pressure (in Pa), $\mathbf{g}$ is the gravity acceleration vector (in m s^{-2}), $\rho(\mathbf{r},t)$ is the macroscopic electrical charge density (C m^{-3}), t is time (in s), and ϕ is the interconnected fractional porosity. Other couplings leading to spontaneous electric potentials are described in *Revil* [1999]. The macroscopic electrical field (in V m^{-1}) is given by

$$\mathbf{E} = -\nabla\varphi - \frac{\partial\mathbf{A}}{\partial t}, \tag{5}$$

where φ is the scalar electrical potential (in V) which contains in the electromagnetic theory an arbitrary additive constant, and $\mathbf{A}$ (in V s m^{-1}) is the magnetic potential vector (in the Coulomb gauge $\nabla\cdot\mathbf{A} = 0$). Equation (1) shows that even in the absence of an electrical current density ($\mathbf{j} = 0$) and in steady state conditions ($\partial\mathbf{A}/\partial t = 0$), there is a macroscopic electrical potential gradient.

This electrical potential gradient is due to the polarization generated by the drag of the excess of charge located in the vicinity of the grain water interface (Figure 1) by the pore water flow. This electrical potential gradient is called "the streaming potential." Equations (1) and (2) are valid only for small forces, at least small enough to neglect any quadratic terms. The elements entering into the matrix ℓ_{ij} are all second-rank symmetrical tensors, whereas ℓ_{ij} itself is a matrix belonging to a mixed affine and metric space [e.g., *Bear*, 1988, p. 89]. The first term of (1) corresponds to Ohm's law, and the second term of (2) represents the Darcy's law. Consequently, we note

$$\ell_{11} = \sigma, \tag{6}$$

$$\ell_{12} = \ell_{21} = \ell, \tag{7}$$

$$\ell_{22} = k/\eta_f, \tag{8}$$

where σ and k are the electrical conductivity (in S) and intrinsic permeability (in m^2) tensors of the porous material, respectively, η_f is the dynamic shear viscosity of the pore fluid, and ℓ is the coupling electrokinetic tensor, which is analyzed in section 3 for isotropic and anisotropic porous materials. We assume that $\sigma, k,$ and ℓ have the same principal directions because they are all related to the same tortuosity tensor of the interconnected pore space. Consequently, if the tortuosity tensor is known from electrical conductivity measurements or from permeability measurements, it can be used to compute the principal directions of the tensor ℓ (see section 3.2). For most porous media, with the exception of highly compacted shales with high specific surface areas like smectite-dominated shale, the hydraulic equation can be decoupled from the electric equation because

$$\left| (k/\eta_f)\left(\nabla p - \rho_f \mathbf{g}\right) \right| \gg \left| \ell \, \mathbf{E} \right|. \tag{9}$$

From (2) and (9) we recover the classical Darcy's law:

$$\mathbf{u} \approx -(k/\eta_f)\left(\nabla p - \rho_f \mathbf{g}\right). \tag{10}$$

The pore water pressure and density are given by

$$p = p_0 + \delta p, \tag{11}$$

$$\rho_f = \rho_0 + \delta\rho_f, \tag{12}$$

where p_0 (in Pa) and ρ_0 (in kg m^{-3}) are the hydrostatic pore fluid pressure and density in a hydrostatic reference state ($p_0 = \rho_0 g z$, where z is the depth), δp is the pore fluid overpressure, and $\delta\rho_f$ is the density perturbation due to temperature, salinity, or fluid pressure variations. Typically, a first order state equation for the fluid is given by

$$\rho_f = \rho_0\left[1 - \alpha_f(T - T_0) + \gamma_f(S - S_0) - \beta_f(p - p_0)\right]. \tag{13}$$

The reference state is characterized by the temperature T_0, the salinity S_0, and the fluid pressure p_0. Additional assumptions are made corresponding to the incompressibility of the pore fluid and the use of the Boussinesq approximation in the equations. From (12) and (13):

$$\delta\rho_f = \rho_0\left[-\alpha_f(T - T_0) + \gamma_f(S - S_0)\right]. \tag{14}$$

Introducing (11) and (12) into (10), yields

$$\mathbf{u} \approx -(k/\eta_f)\left(\nabla\delta p - \delta\rho_f\mathbf{g}\right). \tag{15}$$

From (15) the water mass flux can also be written

$$\mathbf{q} = -(k/\nu_f)\nabla\delta p + \nabla\times\Psi, \tag{16}$$

where $\nu_f = \eta_f/\rho_f$ is the kinematic viscosity of the pore fluid and Ψ is the stream vector potential, which is the three-dimensional analog of the stream function for 2-D problems [*Hirasaki and Hellums*, 1968]. The decomposition corresponding to (16) is useful when numerical modeling is used to solve the differential equations corresponding to free convection [*Holst and Aziz*, 1972]. Comparison between (15) and (16) leads to

$$\nabla\times\Psi = \left(\frac{\delta\rho_f}{\nu_f}\right)k\cdot\mathbf{g}. \tag{17}$$

As Ψ is solenoidal [*Holst and Aziz*, 1972], Ψ is determined from (17) by

$$\nabla^2\Psi = -\nabla\times\left(\frac{\delta\rho_f}{\nu_f}k\cdot\mathbf{g}\right). \tag{18}$$

Taking $\nabla\cdot\mathbf{j} = 0$ and inserting (1) leads to

$$\nabla\cdot(\sigma\cdot\mathbf{E}) = \nabla\cdot\left[\ell\cdot\left(\nabla\delta p - \delta\rho_f\mathbf{g}\right)\right]. \tag{19}$$

In steady state conditions, $\mathbf{E} = -\nabla\varphi$, and the linearity of the equations allows one to split (19) into two equations:

$$\nabla\cdot\left(\sigma\cdot\nabla\varphi_p\right) = -\nabla\cdot\left[\ell\cdot\nabla\delta p\right], \tag{20}$$

$$\nabla\cdot\left(\sigma\cdot\nabla\varphi_c\right) = +\nabla\cdot\left[\nu_f\ell\cdot k^{-1}\cdot\nabla\times\Psi\right], \tag{21}$$

$$\varphi = \varphi_p + \varphi_c, \tag{22}$$

where φ is the total electrical potential distribution due to fluid flow, the potential φ_p is the contribution due to the overpressures, and φ_c is due to free convection. Consequently, the electrical potential distribution is determined by the solution of two scalar Poisson equations with source terms corresponding to pore fluid overpressures and free convection, and the use of the superposition principle. In homogeneous porous materials and small temperature gradients, the contribution from (21) can be neglected, and the only contribution results from the solution of (20).

2.2. Magnetic Field Distribution

We specify now the equation for the magnetic field $\mathbf{H}$, which is related to the magnetic vector potential by $\mathbf{H} = (1/\mu)\nabla\times\mathbf{A}$, where μ is the magnetic permeability. The magnetic permeability of virtually all geologic materials does not vary significantly from the magnetic permeability of free space. The macroscopic laws of Ampere and Faraday are given respectively by

$$\nabla\times\mathbf{H} = \mathbf{j} + \frac{\partial\mathbf{D}}{\partial t}, \tag{23}$$

$$\nabla\times\mathbf{E} = -\mu\frac{\partial\mathbf{H}}{\partial t}. \tag{24}$$

where $\mathbf{D}$ is the dielectric displacement and $\mathbf{D} = \varepsilon\mathbf{E}$, ε is the dielectric tensor of the porous material. Taking the curl of Ampere's law and developing $\nabla \times \nabla \times \mathbf{H}$, we have

$$-\nabla^2\mathbf{H} + \nabla\nabla \cdot \mathbf{H} = -\nabla \times \left[\ell \cdot \left(\nabla\delta p - \delta\rho_f\mathbf{g}\right) - \sigma \cdot \mathbf{E}\right] + \frac{\partial}{\partial t}[\nabla \times (\varepsilon \cdot \mathbf{E})].$$
(25)

Combining (24) and (25), the magnetic field obeys:

$$\nabla^2\mathbf{H} - \sigma\mu\frac{\partial\mathbf{H}}{\partial t} - \varepsilon\mu\frac{\partial^2\mathbf{H}}{\partial t^2} = \nabla \times \left[\ell(\nabla\delta p - \delta\rho_f\mathbf{g})\right].$$
(26)

Equation (26) is a propagation-diffusion type equation for the magnetic field with a source term. As shown in section 3, the coupling term ℓ depends on the porosity, the temperature, and the pH and salinity of the pore fluid. Any variation in these parameters associated with a fluid flow, such that the right side of (26) is different from zero, will generate a magnetic wave (together with an electric wave). Electromagnetic waves lose almost no frequency when they propagate in porous materials [e.g., *Haartsen and Pride*, 1997]. Consequently, they provide information at the top surface of the structure about the transient dynamics of fluid flow. Two characteristic time constants appear in (26): $\tau_c = \sigma \mu L^2$ and $\tau_\varepsilon = L(\varepsilon\mu)^{1/2}$ where L is the characteristic distance from the source. For typical values of ε and σ we have $\tau_\varepsilon \ll \tau_c \sim$ few seconds. In the limit $t \gg \tau_c$, the time-derivative terms can be neglected and the solution is given by the stationary part of (26) [*Majaeva et al.*, 1997]. Using $\nabla \cdot \mathbf{H} = 0$ (because $\mathbf{H} = (1/\mu)\nabla \times \mathbf{A}$) and μ is a constant) and taking (26) in its quasistatic limit (we use also $\nabla \times E = 0$), we obtain

$$\nabla^2\mathbf{H} = \nabla \times \left[\ell \cdot \left(\nabla\delta p - \delta\rho_f\mathbf{g}\right)\right].$$
(27)

Equation (27) can be split to give

$$\nabla^2\mathbf{H}_p = \nabla \times [\ell \cdot \nabla\delta p],$$
(28)

$$\nabla^2\mathbf{H}_c = -\nabla \times \left[v_f\ell \cdot k^{-1} \cdot \nabla \times \Psi\right],$$
(29)

$$\mathbf{H} = \mathbf{H}_p + \mathbf{H}_c.$$
(30)

Here $\mathbf{H}$ is the total magnetic field induced by fluid flow. The magnetic field $\mathbf{H}_p$ is the contribution due to the pore fluid overpressures, and $\mathbf{H}_c$ is due to free convection. Consequently, the magnetic field due to water flow is determined by the solution of two vectorial Poisson equations with source terms corresponding to pore fluid overpressures and free convection and the use of the superposition principle. Assuming the spatial variations of the tensor (ℓ k^{-1}) can be neglected (homogeneous porous materials and small temperature gradients) yields:

$$\mathbf{H}_p = 0,$$
(31)

$$\nabla^2\mathbf{H}_c = -v_f\ell \cdot k^{-1} \cdot \omega,$$
(32)

$$\mathbf{H} = \mathbf{H}_c.$$
(33)

where $\omega \equiv \nabla \times \nabla \times \Psi$ is the vorticity vector. Consequently, the sources for the generation of the magnetic field, in that special case, are the vorticities of the convection pattern. The greater these vorticities are, the greater the associated magnetic field is. These magnetic fields of electrokinetic origin could explain the so-called "volcanomagnetic effect" observed on Piton de la Fournaise Volcano (Réunion Island) by *Zlotnicki and Le Mouel* [1988, 1990]

The electrical and magnetic fields solution of (20)-(22), and (28)-(30) with the appropriate boundary conditions (see section 2.3) have to be added to the electric and magnetic fields due to other sources (e.g., related to the presence of ferromagnetic mineral concentrations, ore deposits, or human activities or due to induction phenomena).

2.3. Boundary Conditions

To close the electrokinetic problem, the boundary conditions for the electrical potential and the magnetic field have to be specified at any boundaries $d\Omega$ of the homogeneous volume Ω in which the solutions of (20)-(22), and (28)-(30) have to be computed. The boundary conditions are

$$\varphi_{(-)}\mid_{d\Omega} = \varphi_{(+)}\mid_{d\Omega},$$
(34)

$$\sigma_{(-)}\frac{\partial\varphi_{(-)}}{\partial n}\mid_{d\Omega} = \sigma_{(+)}\frac{\partial\varphi_{(+)}}{\partial n}\mid_{d\Omega},$$
(35)

$$\mathbf{H}_{(-)}\mid_{d\Omega} = \mathbf{H}_{(+)}\mid_{d\Omega},$$
(36)

$$\frac{\partial}{\partial n}(\mathbf{H}_{(-)} - \mathbf{H}_{(+)})\mid_{d\Omega} = \mathbf{n} \times (\mathbf{j}_{(-)} - \mathbf{j}_{(+)})\mid_{d\Omega},$$
(37)

on the boundaries $d\Omega$, where $\varphi_{(-)}$, $\mathbf{H}_{(-)}$, and $\mathbf{j}_{(-)}$ are the electrical potential, the magnetic field, and the electric current density, respectively, on $d\Omega_{(-)}$, $\varphi_{(+)}$, $\mathbf{H}_{(+)}$, and $\mathbf{j}_{(+)}$ are the electrical potential, the magnetic field, and the electric current density, respectively, on $d\Omega_{(+)}$, and $\partial./\partial n$ is defined by

$$\frac{\partial.}{\partial n} \equiv \mathbf{n}.\nabla(\,.\,),$$
(38)

where $\mathbf{n}$ is a unit vector normal to the boundary and pointing from region (+) into region (-). At the boundaries $d\Omega$ of a geological object in contact with air or a very resistive structure (e.g., sediments in contact with basalts or granites), we consider $\sigma_{(+)} = 0$ and $\mathbf{j}_{(+)} = 0$ ($d\Omega_{(-)}$ being the internal surface and $d\Omega_{(+)}$ being the external surface), so (35) and (37) become

$$\frac{\partial\varphi_{(-)}}{\partial n}\mid_{d\Omega} = 0,$$
(39)

$$\frac{\partial}{\partial n}(\mathbf{H}_{(-)} - \mathbf{H}_{(+)})\mid_{d\Omega} = \mathbf{n} \times \mathbf{j}_{(-)}\mid_{d\Omega}.$$
(40)

If the boundary $d\Omega$ is in contact with water, for example, we have

$$\sigma_{(-)}\frac{\partial\varphi_{(-)}}{\partial n}\mid_{d\Omega} = \sigma_f\frac{\partial\varphi_{(+)}}{\partial n}\mid_{d\Omega},$$
(41)

$$\frac{\partial}{\partial n}(\mathbf{H}_{(-)} - \mathbf{H}_{(+)})\mid_{d\Omega} = \mathbf{n} \times (\mathbf{j}_{(-)} - \mathbf{j}_{(+)})\mid_{d\Omega},$$
(42)

where σ_f is the electrical conductivity of the fluid at the boundary $d\Omega$. Note that if σ_f is high enough to consider the fluid to be a perfect conductor, $d\Omega$ is an equipotential and no self-potential anomalies (or at least very small anomalies) can be observed. For example, *Corwin and Hoover* [1979] reported very small electrical potential anomalies (< 1 mV) measured at the bottom of Mono Lake (California) near the active hot springs area on Paoha Island (the reported electrical conductivity of the highly saline Mono Lake water is 10 S m^{-1}). Consequently, the higher the salinity of the water at the surface of a geological object is, the lower the electrical potential anomalies associated with subsurface pore fluid circulations are. At the opposite, subsurface

fluid flows in lakes with fresh water should exhibit high electrical potential anomalies.

The hydraulic flow rate (in kg s^{-1}) and electrical current (in A m^2) over a surface element S are defined by the fluxes of the vectorial fields $\mathbf{q}$ and $\mathbf{j}$:

$$Q = \iint_S \mathbf{q}.\mathbf{n}\, dS, \tag{43}$$

$$I = \iint_S \mathbf{j}.\mathbf{n}\, dS, \tag{44}$$

where $\mathbf{n}$ is the unit vector normal to the unit surface element dS of S oriented positive outward. For realistic modeling of complex hydrological systems, various boundary conditions can be specified on $d\Omega$. In terms of heat and flow transfer, conductive and/or convective boundary conditions can be chosen, and Q and/or I can be fixed on some section of the boundary $d\Omega$. For example, for the electrical field we can fix the potential $\varphi = Cte$ (Dirichlet boundary condition), or we can fix the electrical current (Neuman boundary condition) on the boundary. Additional boundary conditions have to be chosen for the pore fluid pressure and stream vector potential [see *Hirasaki, and Hellums*, 1968].

3. Material Properties

In this section, we investigate the relationships between the material properties entering the previous macroscopic laws and the microstructure. The influences of pore fluid salinity, pH, temperature, and partial saturation are accounted for in these relationships.

3.1. Isotropic Porous Materials

We first consider an isotropic REV of a water saturated quartz sand characterized by an average grain diameter d and the fractional porosity ϕ. We assume a unimodal grain size distribution, and for spheroidal grains the grain diameter is defined by the diameter of a sphere having the same volume as the grain. The phenomenological coefficients ℓ_{ij} are related to more conventional parameters by

$$\ell_{11} = \sigma = \frac{\sigma_f}{F}\, \mathcal{H}[\xi], \tag{45}$$

$$\ell_{12} = \ell_{21} = -\frac{\varepsilon_f \zeta}{\eta_f F}, \tag{46}$$

$$\ell_{22} = \frac{k}{\eta_f}. \tag{47}$$

Here σ is the electrical conductivity of the REV, σ_f is the pore fluid electrical conductivity, ξ is the ratio of mineral surface and pore fluid electrical conductivity [*Revil and Glover*, 1998], and $\mathcal{H}[\xi]$ is a function of the parameter ξ (the exact expression for $\mathcal{H}[\xi]$ depends on the topology of the interconnected pore space, and we have $\mathcal{H}[\xi \to 0] \to 1$). The parameters F and k are the electrical formation factor and the permeability (in m^2) of the REV, respectively. The parameters ρ_f and η_f are the density and the dynamic shear viscosity of the pore fluid respectively, $\varepsilon_f \approx 80\varepsilon_0$ ($\varepsilon_0 = 8.84 \times 10^{-12}$ F m^{-1}) is the dielectric constant of pore water, and ζ is the so-called "zeta potential" and represents the electrical potential drop through the electrical diffuse layer [see *Revil et al.*, this issue]. Note that sign(ℓ) = -sign (ζ) and $\zeta < 0$, in most of the natural conditions of fluid pH, temperature, and

salinity. Equations (45) and (47) are very general equations defining the electrical conductivity and the permeability. Equation (46) results from the model of *Pride* [1994] and is obtained by volume averaging the Nernst-Planck, Navier-Stokes, and Poisson-Boltzmann equations over the REV (there is a small correction term in the equation of *Pride* [1994], which is neglected in this paper). In clay free sands we can relate the three fundamental parameters (electrical conductivity, permeability, and coupling coefficient) to the microstructure (characterized by d and ϕ):

$$\mathcal{H}[\xi] = 1 - t_{(+)}^f + F\xi + \frac{1}{2}\left(t_{(+)}^f - \xi\right)\left(1 - \frac{\xi}{t_{(+)}^f} + \sqrt{\left(1 - \frac{\xi}{t_{(+)}^f}\right)^2 + \frac{4F\xi}{t_{(+)}^f}}\right), \tag{48}$$

$$k = \frac{d^2}{24\, F(F-1)^2}, \tag{49}$$

where F and ξ are defined by,

$$F \equiv (\phi - \phi_p)^{-m}, \tag{50}$$

$$\xi \equiv \frac{4}{d}\left(\frac{\Sigma_S}{\sigma_f}\right). \tag{51}$$

Equation (48) results from *Revil and Glover* [1998], and (49) results from *Revil and Cathles* [1999]. Equation (50) results from the differential effective medium approach used by *Sen et al.* [1981]; m is called the electrical cementation exponent or Archie's exponent. We have accounted for the effect of the percolation porosity ϕ_p (i.e., the porosity at the percolation threshold, $\phi_p \approx 0.025 \pm 0.025$ for spherical particles depending on the cementation process). At the percolation threshold itself, the physics of percolation rather than the more classical methods leading to Eqs. (48)-(51) should be used to determine the macroscopic properties at a given scale. In (51), Σ_S is the specific surface conductance (in S). The specific surface conductance of the mineral grains characterizes the "excess" (surface) conductivity at the grain surface by comparison with that of the bulk water [e.g., *Revil and Glover*, 1997, 1998]. The parameter $t_{(+)}^f$ is the fraction of electrical electromigration current carried by cations in the bulk electrolyte ($t_{(+)}^f$ is called the "pore fluid Hittorf number of the cations" [e.g., *Revil and Glover*, 1997, 1998, *Revil et al.*, 1998], $t_{(+)}^f \approx 0.38$ for NaCl; $t_{(+)}^f \approx 0.51$ for KCl). The parameter $t_{(+)}^f$ is simply a function of the ionic mobility of the cations and anions in the water phase [*Revil and Glover*, 1997, 1998]. If the grains are perfectly spherical, $m = 1.5$. Usually, $1.3 \leq m \leq 1.7$ (see Figure 2) because the grains are not perfectly spherical. The lower limit for m is characteristic of fractured porous media.

In (48) the tortuosity paths for cations and anions are different at low salinities because only one of the ionic species (anions or cations) has preferential adsorption upon the mineral surface, depending on the thermodynamic conditions of pH, ionic strength, pressure, and temperature [see *Revil et al.*, this issue]. Equation (49) assumes that the average pore radius is given by $\Lambda = d/[3(F-1)]$ as demonstrated by *Revil and Cathles* [1999]. The predictions of (49), in which the formation factor has been replaced by (50), are tested in Figure 3. There is very good agreement between the experimental data and the prediction of the permeability equation over 6 orders of magnitude in permeability.
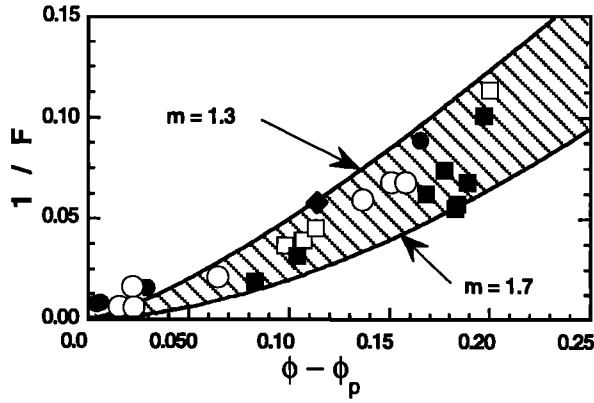
Figure 2. Relationship between the formation factor and the porosity for clay-free sands. Data are from (solid circle) *Sen et al.* [1981], (open square) *Johnson et al.* [1982], (open circle) Revil (unpublished manuscript, 1995), (solid square) *Waxman and Smits* [1968], (diamond) *Schwartz et al.* [1989]. We use $\phi_p = 0.035$.

The fundamental parameter usually used to describe laboratory streaming potential measurements is the "streaming potential coupling coefficient" C (in V Pa^{-1}) defined at steady state conditions by

$$C \equiv \left(\frac{d\varphi}{d\delta p}\right)_{j=0}, \qquad (52)$$

where $\delta p = (p - \rho_0 g z)$ is the pore fluid overpressure and z is the depth (usually, in laboratory experiments the gravity term $\rho_0 g z$ can be neglected and $d\delta p = dp$). Combining (45), (46), and (52) yields

$$C = -\frac{\ell_{12}}{\ell_{11}} = \frac{\varepsilon_f \zeta}{\eta_f \sigma_f}\left(\frac{1}{\mathcal{H}[\xi]}\right), \qquad (53)$$

which is a new equation for the streaming potential coupling coefficient. In the limit $\xi \to 0$ (e.g., at very high salinities), C reduces to the well-known Helmoltz-Smoluchowski equation [e.g., *Dukhin and Derjaguin*, 1974]:

$$C_{HS} = \varepsilon_f \zeta /(\eta_f \sigma_f). \qquad (54)$$

Equation (54) shows no dependence between the streaming potential coupling coefficient and the microstructure. The Helmoltz-Smoluchowski equation is very often used to interpret streaming potential measurements, but this equation can lead to serious errors as shown below. In (53) the dependence of C with the microstructure comes from $\mathcal{H}[\xi]$. The ratio between C and C_{HS} (a normalized streaming potential coupling coefficient) is given by $1 / \mathcal{H}[\xi]$. The high salinity asymptote of $\mathcal{H}[\xi]$ (corresponding to $\xi \ll 1$) is

$$\mathcal{H}[\xi] = 1 + 2\,(F - 1)\,\xi \qquad (55)$$

In such an asymptotic limit, (54) has a form similar to that given by *Morgan et al.* [1989] and *Jouniaux and Pozzi* [1995]. Indeed, (54) and (55) lead to the high salinity asymptotic limit

$$C = \frac{\varepsilon_f \zeta}{\eta_f \sigma_f(1 + 2(F-1)\xi)}. \qquad (56)$$

Replacing ζ with (51) and using the relationship $\Lambda = d/[3(F-1)]$ between the average grain diameter d, the electrical formation factor F, and the mean pore radius Λ yields

$$C \approx \frac{\varepsilon_f \zeta}{\eta_f(\sigma_f + 2\Sigma_s / \Lambda)}, \qquad (57)$$

which is similar to equation (4) of *Morgan et al.* [1989]. We compare our model and the Helmoltz-Smoluchowski equation with the experimental data of *Bull and Gortner* [1932] (Figure 4). *Bull and Gortner* [1932] reported that C decreases with grain size for sand columns composed of crushed quartz grains. There is a good agreement between our model and their experimental data without the help of any adjustable parameters (the ζ potential and the specific surface conductance are given by the model developed by *Revil et al.* [this issue]). The model of *Morgan et al.* [1989] does a better job than the Helmoltz-Smoluchowski equation, but it still does not describe accurately the experimental results displayed in Figure 4. Figure 4 also implies a difference between the streaming potential coupling coefficient of sands and shales. The average grain diameter of the shale grains is in the range 10-0.01 μm. According to Figure 4, a typical sand (say, with a grain diameter in the range 100-200 μm) has a streaming potential coupling coefficient much higher than a shale at the same salinity because the high surface conductivity of shales decreases the streaming potential coupling coefficient. This effect is also reinforced by the fact that the ζ potential of quartz is usually higher than the ζ potential of clays at the same salinity, except at high salinities (see section 3.3).

Most of the time, the fluid flow equation is not corrected for the electro-osmotic contribution (second term of (2)) in order to derive the permeability. Consequently, the permeability reported in most of the experiments is only an "apparent permeability."
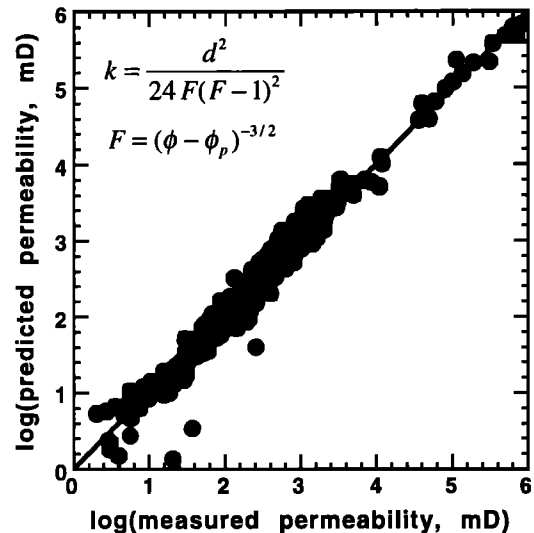

Figure 3. Permeability of clean sands. Comparison between the prediction of the permeability equation described in the main text ($m = 3/2$; $\phi_p = 0.035$) and the experimental results from *Chauveteau and Zaitoun* [1981], *Johnson et al.* [1986], *Chilindar* [1964, Figure 2, p. 73], and *Bear* [1988] (210 samples are used with porosities ranging from 0.056 to 0.43 and grain diameter ranging from 12.5 to 1010 μm). 1 mD = 10^{-15} m^2.
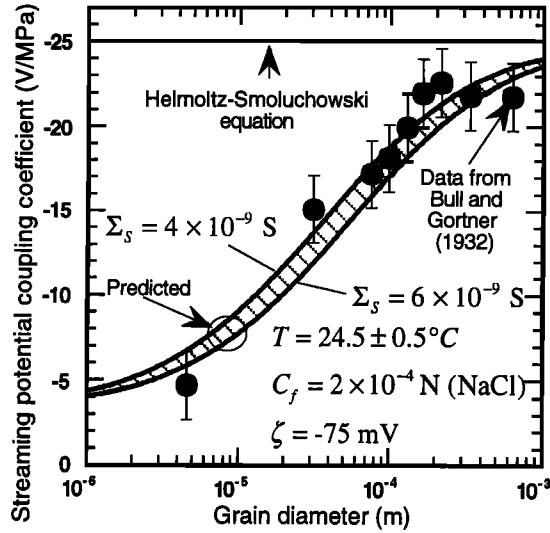
Figure 4. Grain size dependence of the streaming potential coupling coefficient for a quartz sand. The model developed in the main text is compared with the data of *Bull and Gortner* [1932]. We point out that the model is free of any adjustable parameters. The formation factor is estimated from the porosity of a random packing of spheres (i.e., $\phi = 0.38$, [*Chandler*, 1981]) using $F = \phi^{-3/2}$ (see main text). The values of the specific surface conductance and ζ potential are determined from our model [*Revil et al.*, this issue]. Parameters used are as follows: $\sigma_f = 2.41 \times 10^{-3}$ S m^{-1} (determined from the salinity and the temperature; see appendix), $t^f_{(+)} = 0.38$ (NaCl electrolyte), $F = 4.27$ (using Archie's formula), $\zeta = -75$ mV, $\varepsilon_f = (80 \times 8.84) \times 10^{-12}$ F m^{-1}, and $\eta_f = 8.79 \times 10^{-4}$ kg m^{-1} s^{-1}.

The apparent permeability is related to the true (i.e., intrinsic) permeability k by $k^* = k(1 - \mathcal{R})$, where $\mathcal{R}$ is a dimensionless number defined from (1) and (2) as (using $\mathbf{j} = 0$),

$$\mathcal{R} \equiv \frac{\ell_{12}\ell_{21}}{\ell_{11}\ell_{22}} = \frac{24}{\eta_f \sigma_f \mathcal{H}[\xi]} \left[\frac{\varepsilon_f \zeta (F-1)}{d} \right]^2 . \tag{58}$$

Equation (58) is valid only in the limit where $\mathcal{R} \ll 1$ (say $\mathcal{R} < 1/4$), that is in the limit of the thin and locally flat electrical double layer. From (1) and (2) the total energy dissipation function can be written as [e.g., *de Groot and Mazur*, 1962]

$$\mathcal{D} = f^T \mathcal{L} f , \tag{59}$$

where f and $\mathcal{L}$ are the force vector operating over the REV and the material transfer matrix of the REV, respectively, which are defined from (1) and (2) by

$$f = \begin{bmatrix} \mathbf{E} \\ -(\nabla p - \rho_f \mathbf{g}) \end{bmatrix} , \tag{60}$$

$$\mathcal{L} = \begin{bmatrix} \ell_{11} & \ell_{12} \\ \ell_{21} & \ell_{22} \end{bmatrix} . \tag{61}$$

Because $\mathcal{D} \geq 0$ and f is arbitrary, $\mathcal{L}$ must be positive definite, and consequently $| \mathcal{L} | \equiv \ell_{11}\ell_{22} - \ell_{12}\ell_{21} \geq 0$. As $\ell_{12} = \ell_{21}$ (from Onsager's microreversibility principle), the absolute magnitude of the coupling coefficient is restricted by the magnitude of the conductivity coefficients, and we obtain from (45) and (47) the

following: $\ell_{12}^2 \leq \sigma k / \eta_f$, which is also $\mathcal{R} \leq 1$. Consequently, $\mathcal{R}$ obeys the inequality: $0 \leq \mathcal{R} \leq 1$, which is a very general inequality.

In the case of mixtures between quartz sands and clays (Figure 1) the electrical conductivity and the streaming potential coupling coefficient are still given by (45) and (53). However, the non-dimensional parameter ξ is now related to the excess of surface charge per unit pore volume Q_V by [e.g., *Revil and Glover*, 1998]

$$\xi \equiv \frac{\sigma_S}{\sigma_f} \approx \frac{2}{3} \left(\frac{\phi}{1-\phi} \right) \left(\frac{\beta_S Q_V}{\sigma_f} \right) . \tag{62}$$

Here σ_S is the surface conductivity of the grains (in S m^{-1}), ϕ is the interconnected porosity, and β_S (in m^2 s^{-1} V^{-1}) is the mobility of sorbed ions in the electrical double layer. The parameter Q_V (in C m^{-3}) is related to the "cation exchange capacity" (CEC) by [*Waxman and Smits*, 1968]

$$Q_V = \rho_g \left(\frac{1-\phi}{\phi} \right) \varphi_W \, \text{CEC}, \tag{63}$$

where ρ_g is the grain density (in kg m^{-3}) and φ_W is the total mass fraction of clay mineral in the porous material. The CEC (in meq g^{-1} of matrix weight; 1 meq g^{-1} = $(e \, \mathcal{N})$ C kg^{-1} = 96320 C kg^{-1}, $\mathcal{N}$ is Avogadro's number, and e is the elementary charge) indicates the maximum number of surface exchangeable metal ions per unit mass of the rock clay fraction (i.e., the finest grain particles). The CEC is characteristic of the clay mineral type. Typical values are CEC(kaolinite) = 0.04 ± 0.02 meq g^{-1}, CEC(illite) = 0.22 ± 0.02 meq g^{-1}, and CEC(smectite) = 1.5 ± 0.5 meq g^{-1}. For a mixture of clays we can take an arithmetic average with weighting corresponding to the mass fraction of each clay mineral, noted as χ_i, that is CEC(clay) = Σ_i (χ_i CEC$_i$). Note that for zeolites, the CEC is not the relevant parameter for computing the surface conductivity. Zeolites are crystalline aluminosilicates with a tetrahedral framework enclosing cavities occupied by cations having enough freedom of movement to permit cation exchange. However, *Clavier et al.* [1984] showed that some zeolites have large CEC values but no surface conductivity at all. *Olhoeft* [1986] reported that clinoptilolite, the most common zeolite, behaves like kaolinite or montmorillonite, depending on the salinity and temperature. Additional experimental data concerning the surface properties of zeolites are needed to understand and to classify the electrical properties of these minerals, which are always present in geothermal areas.

3.2. Anisotropic Porous Materials

The coupling coefficient ℓ is a second-rank symmetrical tensor in anisotropic porous materials and can be obtained by generalizing the previous equation to anisotropic porous materials. The coupling coefficient ℓ is given by

$$\ell = -\left(\frac{\varepsilon_f \zeta}{\eta_f} \right) \mathbf{G}, \tag{64}$$

$$\mathbf{G} = \mathbf{T} \, \phi, \tag{65}$$

where $\mathbf{T}$ is an extension of the tortuosity concept to 3-D flow and anisotropic porous media [*Bear*, 1988, p. 111] (note that in the principal directions, the main components of $\mathbf{T}$ are smaller than unity). The anisotropy of the electrical conductivity σ, the permeability k, and the coupling coefficient ℓ is actually due to the anisotropy of the tortuosity of the interconnected pore space, and the principal directions of these three tensors are considered

to be the same. The components of the tortuosity tensor can be determined from normalized electrical field integrals [*Avellaneda and Torquato*, 1991]. In isotropic porous media, **G** reduces to

$$G = (1/F)\,I, \tag{66}$$

$$T = (1/\tau^2)\,I, \tag{67}$$

where **I** is the unit tensor, τ is the electrical tortuosity (≥ 1), and F is the electrical formation factor.

3.3. Influence of the Pore Water pH and Salinity

Because the coupling term ℓ depends directly on the ζ potential and the specific surface conductance, these parameters play a central role in any evaluation of the electrokinetic properties of porous rocks. The ζ potential and the specific surface conductance depend on several parameters including the mineral type, the water composition and ionic strength, the pH, and the temperature. For simple supporting pore electrolyte and silica grains the ζ potential and the specific surface conductance can be determined by the model described in the previous paper

of this series [*Revil et al.*, this issue]. For more complex electrolyte compositions and/or for other minerals, the situation is more complicated. We propose that the ζ potential in clay dominated porous materials can be determined by the following empirical equations (see Figure 5):

$$\zeta(pH,\,I) = \zeta_m \sin\left[\frac{\pi}{12}\Delta pH\right], \tag{68}$$

$$\zeta_m(I) = a + b\,\log_{10} I, \tag{69}$$

$$\Sigma_S(pH,T) = \Sigma_S^m(T)\left|\sin\left(\frac{\pi}{12}\Delta pH\right)\right|, \tag{70}$$

where I is the ionic strength (~salinity) of the pore fluid (in mol L^{-1}), $\Delta pH \equiv pH - pH(pzc)$, $pH(pzc)$ is the value of the pH corresponding to $\zeta = 0$ (point of zero charge (pzc); see Figure 5), ζ_m and Σ_S^m represent the value of the ζ potential and the specific surface conductance, respectively, at pH-$pH(pzc) = 6$ (for oxides, ζ_m varies with the salinity), $a = -26.4$ and $b = 6.24$. The specific surface conductance Σ_S^m is given by $\Sigma_S^m(25^\circ C) \approx (2.5 \pm 0.5) \times 10^{-9}$ S [e.g., *Revil and Glover*, 1998]. Equation (68) represents
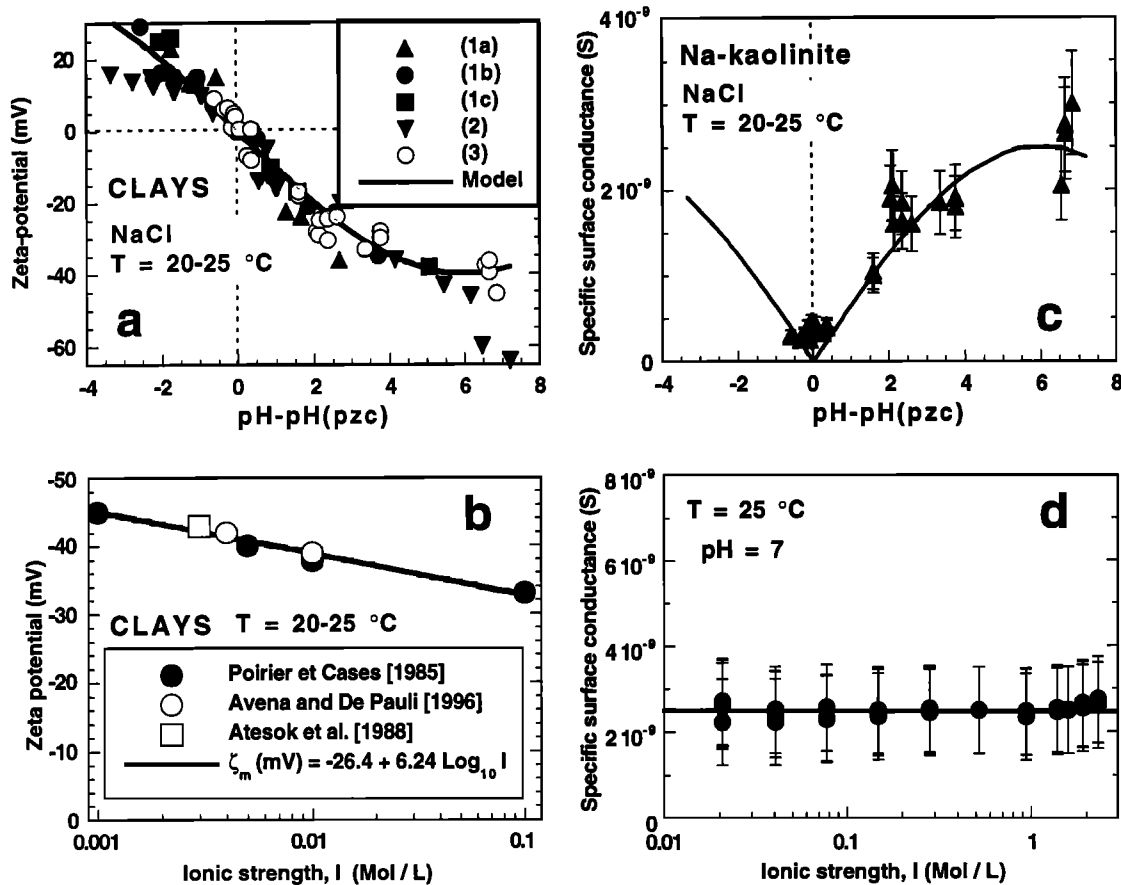

Figure 5. Zeta potential and specific surface conductance of clay minerals: (a) Zeta potential (mV) versus pH (clays, NaCl electrolyte). (1a-1c) *Avena and De Pauli* [1996], for amorphous aluminosilicate, $pH(pzc) = 5.1\pm 0.1$ ($pH(pzc)$ represents the pH corresponding to zero surface charge), (1a) 0.001 M, (1b) 0.004 M, (1c) 0.01 M; (2) *Atesok et al.* [1988]; 0.003 M, Na-kaolinite, $pH(pzc) = 4.75 \pm 0.1$. (3) *Lorenz* [1969], (0.6-2) x 10^{-3} M, Na-Kaolinite, $pH(pzc) = 4.15 \pm 0.1$, (b) zeta potential (mV) at pH - $pH(pzc) = 6$ versus ionic strength (in M) (some of the values are extrapolated from close pH values), (c) specific surface conductance (in S) of Na-kaolinite versus pH (the data points are determined from Figures 6 and 7 of *Lorenz* [1969], salinity: (0.6-2) x 10^{-3} M, Na-Kaolinite, $pH(pzc) = 4.15 \pm 0.1$), and (d) Specific surface conductance (in S) determined from the electrical conductivity measurements of *Waxman and Smits* [1968, Table 7, samples 17, 23, 24, and 26], the electrical conductivity model of *Revil and Glover* [1998], and a surface site density of 3 sites nm^2.

quite well the sigmoid shape of the ζ-pH curves as shown for various clay minerals in Figure 5 with simple supporting pore electrolyte like NaCl or KNO$_3$. The influence of the temperature upon ζ and Σ_S is discussed in section 3.4.

3.4. Influence of the Temperature

The temperature dependence of the ζ potential of quartz has been analyzed in the previous paper of this series [Revil et al., this issue]. The temperature dependence of the electrical conductivity and dielectric constant of the electrolyte (NaCl) are given in the appendix. Typically, the temperature dependence of the electrolyte and surface conductivities can be expressed in linear form, which describes laboratory measurements very well [Revil et al., 1998]:

$$\sigma_f(T) = \sigma_f(T_0)\left[1 + \alpha_f(T - T_0)\right],$$ (71)

$$\Sigma_S(T) = \Sigma_S(T_0)\left[1 + \vartheta_S(T - T_0)\right],$$ (72)

where T_0 is a reference temperature (25°C), $\vartheta_f \approx 0.023°C^{-1}$ and $\vartheta_S(Na^+) \approx 0.040 \pm 0.002°C^{-1}$. Because $\vartheta_S > \vartheta_f$, the ratio of the surface conductivity to the electrolyte conductivity, ξ, increases with the temperature. Equations (45)-(48) and (55), yield in the high salinity domain ($\xi \ll 1$)

$$\frac{d\sigma}{dT} = \frac{1}{F}\left(\sigma_f(T_0)\vartheta_f + 2(F-1)\sigma_S(T_0)\vartheta_S\right).$$ (73)

$$\frac{d\ell}{dT} = \left(\frac{\partial\ell}{\partial\zeta}\right)\frac{d\zeta}{dT} + \left(\frac{\partial\ell}{\partial(1/\eta_f)}\right)\frac{d(1/\eta_f)}{dT}.$$ (74)

$$\frac{\partial\ell}{\partial\zeta} = -\frac{\varepsilon_f}{\eta_f(T)F},$$ (75)

$$\frac{\partial\ell}{\partial(1/\eta_f)} = -\frac{\varepsilon_f\zeta(T)}{F}.$$ (76)

We expand ζ and $1/\eta_f$ to the first order with temperature:

$$\zeta(T) = \zeta(T_0)\left(1 + \vartheta_\zeta(T - T_0)\right),$$ (77)

$$1/\eta_f(T) = 1/\eta_f(T_0)\left(1 + \vartheta_\eta(T - T_0)\right).$$ (78)

$$\frac{d\zeta}{dT} = \zeta(T_0)\vartheta_\zeta,$$ (79)

$$\frac{d}{dT}\left(\frac{1}{\eta_f}\right) = \frac{1}{\eta_f(T_0)}\vartheta_\eta.$$ (80)

The temperature coefficient ϑ_ζ is obtained from the analysis given by Revil et al [this issue] and is ~1.71 x 10^{-2} °C^{-1} for quartz. The temperature coefficient ϑ_η has been calculated using the expression developed by Mercer et al. [1975] for the water viscosity in geothermal fields as $\vartheta_\eta \approx 3.12 \times 10^{-2}$ °C^{-1} (for $0 \le T \le 300°C$). Combining the previous equations, and after some algebraic manipulations, we obtain in the high salinity domain ($\xi \ll 1$)

$$\frac{d\ell}{dT} = \ell(T_0)\left(\vartheta_\zeta + \vartheta_\eta + 2\vartheta_\zeta\vartheta_\eta(T - T_0)\right).$$ (81)

We have used these dependences together with the modeling of the temperature dependence of ζ [Revil et al., this issue] to determine the temperature dependence of the streaming potential coupling coefficient C for the case in which either the electrolyte

conductivity or the surface conductivity is dominant (Figure 6). If we had considered the ζ potential to be independent of temperature, the streaming potential coefficient would have decreased slightly with temperature. Using a salinity of 1 mol L^{-1}, our model indicates $\zeta = -0.035$ mV at 25°C and $C = -(21 \pm 1)$ mV atm^{-1} (~0.2 V MPa^{-1}), coincident with the value of -21 mV atm^{-1} measured by Morgan et al. [1989; Figure 11] for crushed Westerly granite in contact with a NaCl solution ($C_f = 1$ mol L^{-1} and $T = 25°C$). Using these values and the temperature dependence of ζ with T [Revil et al., this issue], the streaming potential coupling coefficient increases in magnitude by about 0.16-0.33 mV atm^{-1} °C^{-1} in the temperature range 25°-70°C. This is in contradiction with the data reported by Morgan et al. [1989] (which assume no temperature dependence of the ζ potential) but in agreement with the data of Ishido and Mizutani [1981] (which leads to a temperature dependence of the ζ potential). A comparison between the predictions of our model and the data of Ishido and Mizutani[1981, their Figure 9] is given in Figure 7. Because the experiment of Ishido and Mizutani was conducted on crushed quartz, we have neglected the surface conductivity in our model for $C(T)$ because of the significant size of the pores. There is a very good agreement between the model and experimental data, indicating that the ζ potential increases with temperature. We believe that this temperature dependence was not observed by Morgan et al. [1989] because of the major difference between the two works in the equilibration time, which is much smaller (4 hours) in the experiment of Morgan et al. [1989] than in the experiment of Ishido and Mizutani [1981] (> 43 hours). Consequently, chemical equilibrium on a silica surface is implied to take several tens of hours when the temperature is
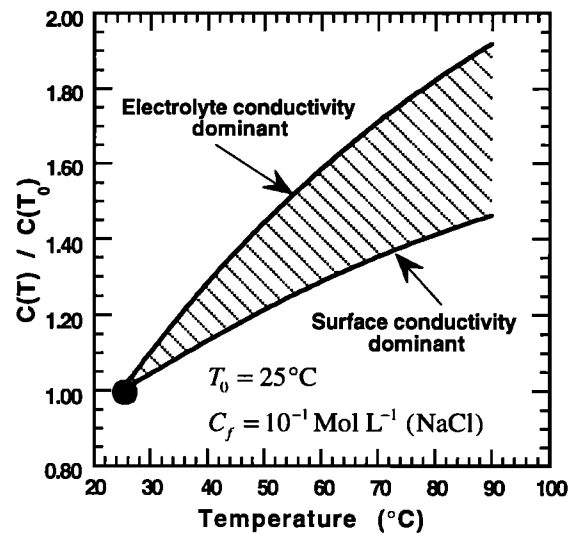

Figure 6. Temperature dependence of the streaming potential coupling coefficient. When the electrolyte salinity is such that pore water electrical conduction remains the dominant mechanism of electrical conduction in the temperature range considered, the temperature dependence of C is much more important than the case where surface conductivity is the dominant mechanism. This is because the temperature dependence of surface conduction is greater than the temperature dependence of bulk conduction in the pore fluid and because the electrical conductivity term is in the denominator of the expression describing the streaming potential coupling coefficient.
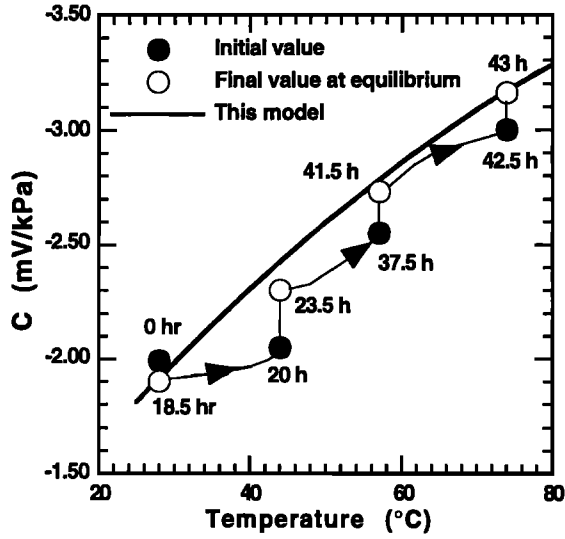
Figure 7. Variation of the streaming potential coupling coefficient as a function of temperature. We compare here the theoretical model described in the main text with the experimental data of *Ishido and Mizutani* [1981] obtained for crushed quartz (pH = 6.1, and 10^{-3} KNO_3). The numbers attached to the experimental points indicate the elapsed time from the beginning of the experiment to each measurement.

changed. We have introduced here the temperature dependence for all parameters of the streaming potential coupling coefficient. We determine in section 3.5 the influence of a gas phase upon C.

3.5. Influence of Gas Saturation

The presence of gas or oil (or any non-wetting and insulating phase) in the interconnected pore space has a significant effect upon the streaming coupling coefficient [e.g., *Morgan et al.*, 1989; *Sprunt et al.*, 1994]. Published experimental works show that there is an increase of the streaming potential coupling coefficient C with the gas saturation (1- S_w) (where S_w is the relative volume fraction of the interconnected pore space saturated by water, i.e., the "water saturation"). *Morgan et al.* [1989] showed that C can be enhanced by a factor of 3 or 4 because of the presence of gas in the interconnected pore space. The streaming potential coupling coefficient in an oil-rock system is much higher than in a water-rock system [*Rutgers et al.*, 1959]. *Sprunt et al.* [1994] showed that air bubbles increase C by more than 2 orders of magnitude but that the voltage produced is unstable (note that this instability is probably the result of gas bubbles trapped in the electrodes). *Antraygues and Aubert* [1993] showed that the flow of wet steam in sands at elevated temperatures leads to the generation of significant streaming potentials, and *Marsden* [1987] and *Sprunt et al.* [1994] that the flow of dry steam in porous materials does not produce substantial streaming potentials.

There are two effects to consider when we are dealing with presence of gas bubbles in the pores. The gas bubbles are electrical insulators, but they also carry along their outer surfaces a deficiency of charge that is responsible for a negative bubble surface electrical potential. However, this effect remains poorly understood. *Graciaa et al.* [1995] measured a ζ potential of -65 mV in deionized water for small air bubbles, and *Jarvis* [1972] reported a variation of -20 mV for the surface potential at the air-

water interface in the presence of NaCl and for a salinity variation between infinite dilution and 6 mol L^{-1}. *Sprunt et al.* [1994] cite the work of *Okada and Akagi* [1987] concerning ζ-potential measurements in the presence of gas bubbles which concludes that, in NaCl and $CaCl_2$ solutions, the ζ potential of gas bubbles is always negative and becomes increasingly negative with decreasing salinity. In presence of $Al_2(SO_4)_3$, gas bubbles have a positive ζ potential, hence a positive surface charge, maybe as the result of Al^{3+} sorption. This surface charge associated with the gas bubbles is not taken into account in the following analysis. The only effect accounted for is the insulating role of gas bubbles upon the electrical conductivity and the coupling coefficient.

The influence of gas saturation upon the electrical conductivity can be taken into account by introducing the following transformation into the electrical conductivity equation [*Waxman and Smits*, 1968; *Clavier et al.*, 1984]:

$$\begin{cases} \phi^m \to \phi^m S_w^n \\ Q_V \to Q_V / S_w \end{cases}, \tag{82}$$

where n is called the saturation or second Archie's exponent ($n \approx m$) [*Waxman and Smits*, 1968]. Consequently, from (45), (48), and (82) the electrical conductivity as a function of the water saturation is given by

$$\sigma = \frac{\sigma_f S_w^n}{F} \left[1 - t_{(+)}^f + \frac{F\xi}{S_w^{n+1}} + \frac{1}{2}\left(t_{(+)}^f - \frac{\xi}{S_w}\right) \right.$$

$$\left. \times \left(1 - \frac{\xi}{t_{(+)}^f S_w} + \sqrt{\left(1 - \frac{\xi}{t_{(+)}^f S_w}\right)^2 + \frac{4F\xi}{t_{(+)}^f S_w^{n+1}}}\right) \right]. \tag{83}$$

A plot of σ / σ_f versus ξ for different water saturations is given in Figure 8a. Because water is the wetting fluid, and because we consider gas saturation to be small enough so that the electrical double layer is not perturbed by the presence of gas in the pore space, the streaming potential coupling term ℓ_{12} should not be strongly affected by the presence of gas. This is because this coefficient represents the drag of the excess of the charge of the electrical double layer during fluid flow, which is not influenced by the presence of gas. Consequently ℓ could be essentially independent of the gas saturation. In addition, the transformation corresponding to (82) is valid only if the pore fluid is at rest. However, the streaming potential corresponds to a dynamic phenomenon related to fluid flow. Consequently, there is no streaming potential if the water saturation is below a critical level corresponding to the so-called "irreducible water saturation" S_{w0} ($S_{w0} \approx 0.1$-0.3 for sands and shales) because there is no longer flow of the wetting phase below this limit. Consequently, the water saturation must be replaced by the "effective" or "reduced" water saturation defined by [e.g., *Bear*, 1988, p. 446]:

$$S_e \equiv \begin{cases} \dfrac{S_w - S_{w0}}{1 - S_{w0}} & \text{as } S_w \geq S_{w0}, \\ 0 & \text{as } S_w < S_{w0}. \end{cases} \tag{84}$$

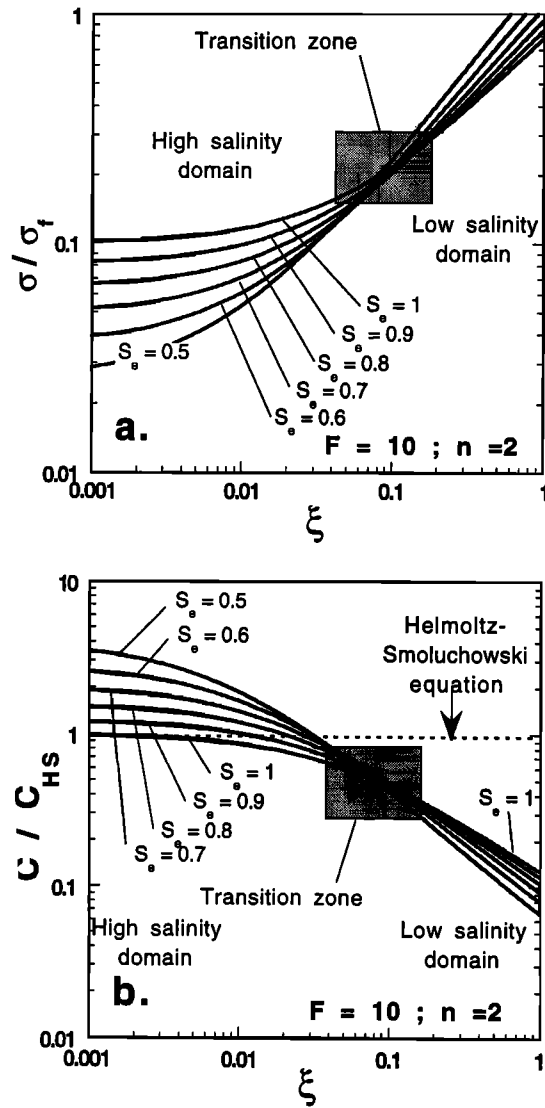Consequently, the streaming potential coupling coefficient is given by

$$C = \frac{C_{HS}}{S_e^2 \left(1 + 2\left(\frac{F}{S_e^2} - 1\right)\frac{\xi}{S_e}\right)}.$$ (86)

The curves C/C_{HS} versus water saturation are shown in Figure 9. The presence of gas in the pore space can lead to a strong enhancement of the streaming potential of several orders of magnitude. This is in agreement with the experimental data of *Jiang et al.* [1998], who noted that the streaming potential coupling coefficient of Red Navajo sandstone samples saturated with oil is about 2 orders of magnitude larger than those saturated by a 0.1 mol L^{-1} brine. The characteristic water saturation at which the streaming potential coupling coefficient is maximum (see Figure 9) is given by the condition $d(C/C_{HS})/dS_w = 0$, which corresponds to $S_w^C \approx S_{w0} + (1 - S_{w0})(F\xi)^{1/3}$. The model presented here is consistent with the experimental observations concerning the streaming potential generated by water/gas flow [*Rutgers et al.*, 1959; *Antraygues and Aubert*, 1993]. A direct comparison between the previous model and experimental data is currently impossible because there are no data in which the streaming potential coupling coefficient is given as a function of gas saturation.

4. Application to Geothermal Fields

In this section we analyze the order of magnitude of the streaming potential anomalies associated with geothermal environments. However, before to deal with these electrical anomalies, we have to point out that recorded field data have to be corrected for extraneous electrical potential variations. Indeed, the electrical potential variations recorded between two electrodes
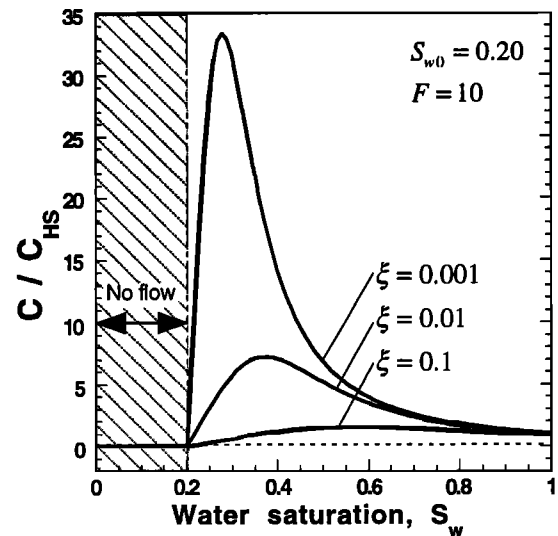

Figure 8. (a) Macroscopic electrical conductivity (normalized by the pore fluid conductivity) versus ξ for different values of the water saturation. (b) Normalized streaming potential coupling coefficient versus the normalized surface conductivity ξ for different water saturations. In the high-salinity domain the decrease of the water saturation is responsible for an increase of the coupling coefficient, whereas in the low-salinity domain the opposite occurs.

$$C = C_{HS}\frac{1}{S_e^n}\left[1 - t_{(+)}^f + \frac{F\xi}{S_e^{n+1}} + \frac{1}{2}\left(t_{(+)}^f - \frac{\xi}{S_e}\right)\right]$$

$$\times\left(1 - \frac{\xi}{t_{(+)}^f S_e} + \sqrt{\left(1 - \frac{\xi}{t_{(+)}^f S_e}\right)^2 + \frac{4F\xi}{t_{(+)}^f S_e^{n+1}}}\right)^{-1}.$$ (85)

Here $C_{HS} \equiv \zeta \varepsilon_f / \eta_f \sigma_f$. A plot of the normalized coupling coefficient C/C_{HS} versus ξ for different effective water saturations is given in Figure 8b. When the gas saturation increases (i.e., S_w decreases), the ratio of the electrolyte conductivity to the surface conductivity decreases and surface conductivity quickly predominates. In the high-salinity domain ($\xi \ll 1$), (85) reduces to

Figure 9. Normalized streaming potential coupling coefficient versus water saturation in the high-salinity domain ($\xi \ll 1$). The streaming potential increases with the decrease of the water saturation from unity to a characteristic value, which depends on the value of ξ. Below this characteristic water saturation the streaming potential coupling coefficient decreases with the decrease of the water saturation until the irreducible water saturation is reached. Below this level, there is no flow of the water phase, and, consequently, no streaming electrical potential can be generated.

in the ground can have various origins. Self-potential monitoring performed for the purpose of detecting electrical potential anomalies of electrokinetic nature has to be corrected from electrical telluric potential variations caused by the magnetic induction in the Earth. This is because the self-potential variations caused by the magnetic induction can be high enough to mask any self-potential variations of electrokinetic nature. To remove the former, *Kawakami and Takasugi* [1994] successfully applied the Wienner filter to self-potential variations in time on the basis of the magnetic field variations and the normalization method using the self-potential reference data points. They show that using this method, the accuracy of the self-potential data of electrokinetic origin was improved from over ±30 mV to ±2-3 mV.

4.1. General Considerations

In the case of ideal free convection, fluid flow is coupled with the temperature field. High temperature fluids tend to rise and cooler fluids tend to move downward because of buoyancy forces. If an electrical diffuse layer exists at the pore matrix interface (Figure 1), all or part of this electrical diffuse layer is carried along by the fluid flow. The transport of the excess charge density contained in the electrical diffuse layer is the source of a macroscopic polarization phenomenon. This process results in an electrical potential gradient. We use the Boussinesq approximation (the fluid density is regarded as temperature dependent in the body forces but is constant elsewhere in the equations). The relationship between the fluid density and the temperature is written as $\rho_f(T) = \rho_f(T_0)[1 - \alpha_f(T - T_0)]$, where $\rho_0 \equiv \rho_f(T_0)$ is the reference fluid density at the reference temperature T_0 and α_f is the thermal volume expansion of water ($\alpha_f \equiv (1/V_f)(\partial V_f / \partial T)_p$). We neglect the fluid pressure gradient in excess of the hydrostatic pressure for upward flow driven by the buoyancy of the hot water, that is $p \approx \rho_0 g z$. Consequently $\nabla p - \rho_f \mathbf{g} \approx \alpha_f(T - T_0)\rho_0 \mathbf{g}$ [*Turcotte and Schubert*, 1982, p. 402]. From (1), the thermoelectrokinetic field is given by,

$$\mathbf{E} = \frac{1}{\sigma}\mathbf{j} + C\alpha_f(T - T_0)\rho_0 \mathbf{g}. \qquad (87)$$

Our purpose is to obtain here an order of magnitude estimate for the thermal electrokinetic effect in geothermal fields. Let us consider the simple case of one-dimensional advection of heat in a porous medium with z denoting depth. We note T_S the surface temperature, T_r the reservoir temperature, and H the depth of the reservoir. For steady state conditions the temperature distribution, the Darcy velocity, and the electrical potential anomaly at the surface of the geothermal field corresponding to the upflow of hot water are given by [*Revil and Pezard*, 1998]

$$T = T_S - (T_S - T_r)\left(\frac{1 - \exp[-\mathrm{Ra}(z/H)]}{1 - \exp(-\mathrm{Ra})}\right), \qquad (88)$$

$$\mathbf{q} = -\frac{k}{\eta_f}\alpha_f \rho_0 (T_r - T_S)\mathbf{g} \qquad (89)$$

$$\delta\psi(0) = -\alpha_f \rho_0 g(T_r - T_S)CH. \qquad (90)$$

where Ra is the Rayleigh number, given by

$$\mathrm{Ra} \equiv \frac{\alpha_f g(\rho_0)^2 k H c_f(T_r - T_S)}{\eta_f \lambda}, \qquad (91)$$

where λ is the effective thermal conductivity of the porous material and $(\rho_0 c_f)$ is the heat capacity of the pore fluid. Symmetrically, the downward flow of cold water driven by the buoyancy forces also creates a self-potential anomaly with the temperature distribution, the Darcy velocity, and the surface self-potential flow given by

$$T = T_S - (T_S - T_r)\left(\frac{1 - \exp[\mathrm{Ra}(z/H)]}{1 - \exp(\mathrm{Ra})}\right), \qquad (92)$$

$$\mathbf{q} = \frac{k}{\eta_f}\alpha_f \rho_0 (T_r - T_S)\mathbf{g}, \qquad (93)$$

$$\delta\psi(0) = \alpha_f \rho_0 g(T_r - T_S)CH. \qquad (94)$$

The ζ potential of silica, under typical geophysical conditions of pH, temperature and salinity, is negative in the absence of strong adsorption phenomena [e.g., *Ishido and Mizutani*, 1981]. In such a case the upwelling flow associated with a hot thermal plume generates a positive thermoelectrokinetic anomaly at the surface of a geothermal field, whereas the downwelling flow associated with a cold thermal plume generates a negative thermoelectrokinetic anomaly (Figure 10). Such self-potential bipolar anomalies can be associated with the fluid flow pattern of active volcanoes (Figure 11) (except that there is an additional effect due to the variation of the water table with the topography [e.g., *Ishido et al.*, 1997; *Sasai et al.*, 1997]). Furthermore, *Zlotnicki and Le Mouel* [1988, 1990] show very convincing examples of strong correlation between magnetic field variations (up to 10 nT) and volcanic activity at la Fournaise volcano (Réunion Island). We believe that these magnetic anomalies are electrokinetic in nature and associated with the vorticity of the fluids convection pattern inside the volcano. Bipolar self-potential anomalies are observed by *Anderson and Johnson* [1976] in the Long Valley Caldera, California, by *Antraygues and Aubert* [1993] around an active fissure on Mount Etna, Italia, by *Sasai et al.* [1997] on Miyakejima Island, Japan, and, recently, by *Michel and Zlotnicki* [1998] on the cone of La Fournaise volcano, Réunion Island, Indian Ocean and by *Lénat et al.* [1998] on Karthala volcano, Grande Comore (Indian Ocean). The wavelengths associated with the thermal convection cells and flow pattern would be equal to the size of the self-potential anomalies. Dipolar anomalies of ± 80 mV in the Cerro Prieto geothermal field, Baja California, Mexico [*Fitterman and Corwin*, 1982], +20/-40 mV at Red Hill Hot Spring, Utah [*Sill*, 1983], and +100/-200 mV in Ergani, Turkey [*Abdelrahman and Sharafeldin*, 1997] have been observed. *Revil and Pezard* [1998] conclude that predictions based on (90) compare well with measured field data by *Fitterman and Corwin* [1982] for the Cerro Prieto geothermal field.

Our model also predicts that positive self-potential anomalies should be associated with less resistive formations and negative self-potential anomalies are associated with more resistive formations. This is because (1) from (88) and (92), the temperature distribution is perturbed by the hydrothermal flow and (2) electrical resistivity decreases with the increase of the temperature according to (73). This is also in agreement with the field data of *Anderson and Johnson* [1976]. We now turn our attention to the question of how the salinity affects the intensity of the self-potential anomalies. The ζ potential decreases with the salinity [*Revil et al.*, this issue], whereas the electrical conductivity increases with salinity. Consequently, the electrokinetic coupling coefficient decreases with the salinity
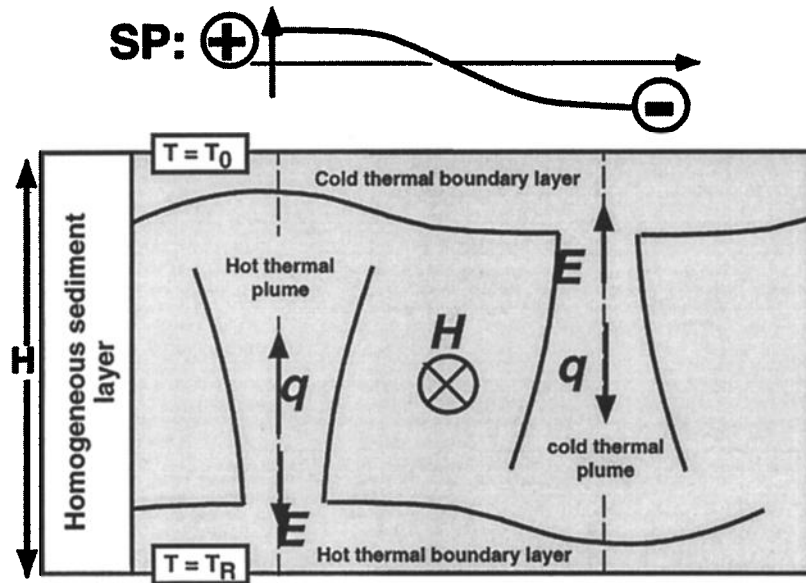
Figure 10. Electric and magnetic fields of electrokinetic nature associated with a geothermal convective cell. A positive electrokinetic anomaly is associated with the rising of hot and saline fluids, whereas a negative anomaly is associated with the downwelling of less saline, colder fluids.

because of the combination of these two effects and as shown by experimental data [e.g., *Hernandez et al.*, 1995, Figures 11 and 12]. It follows that the intensity of the self-potential anomalies of electrokinetic nature decreases with salinity. As a consequence we expect that the percolation of meteoritic water should be associated with streaming potential anomalies greater than those related to the upward flow of very saline water. This seems to be the case for the dipolar anomalies reported by *Anderson and Johnson* [1976], *Fitterman and Corwin* [1982], and *Abdelrahman and Sharafeldin* [1997].

4.2. The Case of Cerro Prieto

We discuss now more extensively the case of the Cerro Prieto geothermal field. This geothermal field is located in the alluvial plain of the Mexicali Valley, northern Baja California, Mexico, at about 35 km southeast of the city of Mexicali. The Cerro Prieto geothermal field is one of several high-temperature water-dominated geothermal fields within the Salton Trough, a complex rift valley between the North American and Pacific plates. This field is used to produce electricity (720 MW electric power) from reservoirs up to 4000 m deep. Because of the extensive international program of collaborative investigation, Cerro Prieto is considered to be one of the best studied geothermal fields in North America. The relationship between the self-potential distribution, the temperature versus depth distribution, and the flow pattern on a southwest to northeast profile (from well M6 to well M53) is analyzed in Figure 12. The self-potential profile was measured in December 1977 and March 1978 [see *Corwin and Hoover*, 1979]. The temperature distribution (Figure 12b) is based on the calcite-water oxygen isotope geothermometer from cores extracted from the boreholes shown in Figure 12b (modified from *Elders et al.* [1983]). The temperature distribution shows a broad area of temperature inversion in the southwest because of a zone of horizontal hot brine flow. The fluid flow pattern is shown in Figure 12c (modified from *Elders et al.* [1983]). The positive
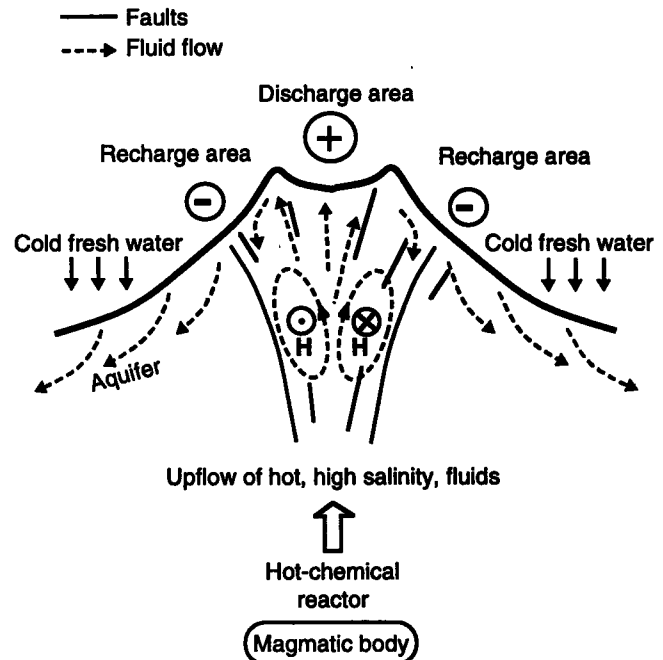

Figure 11. Electrical potential anomalies and magnetic fields of electrokinetic nature associated with an active volcano. The flow pattern is taken from *Michel and Zlotnicki* [1998]. If the *p*H of the fluid is higher than the *p*H(pzc) of the minerals controlling the electrokinetic properties, a positive electrokinetic anomaly is associated with the rising of hot and saline fluids in the central caldera. Negative self-potential anomalies are associated with the downwelling of less saline and colder fluids around the caldera through a concentric pattern of fractures. The hydrothermal cell is also responsible of an electrokinetic magnetic field that is added to magnetic fields of other origins.
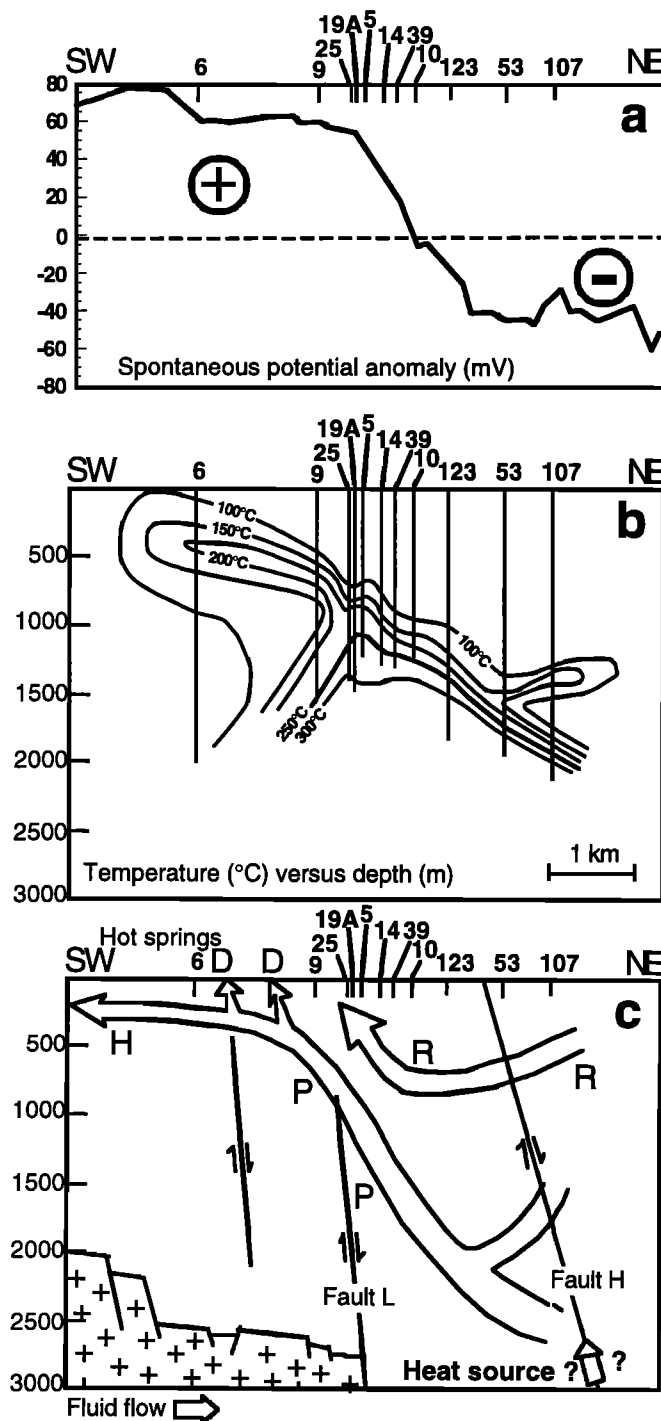
Figure 12. Relationship between the self-potential distribution at the top surface of Cerro Prieto, the temperature versus depth distribution, and the assumed flow profile on a southwest to northeast profile from well M6 to well M53: (a) Self-potential profile measured at the top surface (z = 0) of the Cerro Prieto geothermal field (measured in December 1977 and March 1978, modified from *Corwin and Hoover* [1979]), (b) temperature versus depth distribution based on the calcite-water oxygen isotope geothermometer (modified from *Elders et al.* [1983]); the temperature distribution shows a broad area of temperature inversion in the southwest because of a zone of horizontal hot brine flow, and (c) flow regime (modified from *Elders et al.* [1983]). R is the recharge zone; P is the thermal plume zone; D is the discharge zone; and H is the horizontal flow zone. We add the approximate position of the faults and the basement.

self-potential anomaly is clearly related to the presence of a fluid discharge zone of the hydrothermal system, whereas the negative self-potential anomaly is clearly related to the presence of a hydrothermal recharge zone. Numerical modeling of the heat and fluid flow patterns and self-potential distribution in this geothermal field will be analyzed in a future paper.

4.3. Numerical Modeling

The hydraulic and electromagnetic equations were implemented in the 3-D finite element BasinLAB™ software package. This software is already able to solve complex thermohydraulic problems using realistic geological structures evolving with time. BasinLAB™ is able to handle the presence of faults, complex geological bedding, compaction of sediments, multiphasic flow, free and forced convections, and geochemical equilibria between the pore water and the rock forming minerals. The numerical procedure is based on the Galerkin method on quadrilateral elements with linear basis functions. *Roberts et al.* [1996] discussed numerical stability and tests for the thermo-hydraulic equations. The equations at each time step are solved in the following order. (1) Heat and fluid flow equations [e.g., *Roberts et al.*, 1996], (2) computation of the source for the electric potential problem using the solution to (1), and (3) determination of the electrical potential distribution using equations (20) to (22). In this paper, we show only a simple 2-D case corresponding to the cooling of an impermeable dike intrusion. A typical self-potential distribution is shown in Plate 1 (corresponding to 150 Kyr, after the dike intrusion). A bipolar self-potential distribution is obtained at the open top surface of the structure with a positive self-potential anomaly surrounded by two negative self-potential anomalies. The positive anomaly shows one of these "discharge area" by analogy with what was found for Cerro Prieto. More realistic simulations will be presented in a future paper.

5. Conclusions

The electric and magnetic fields generated by the flow of pore fluids in geothermal systems are investigated in the quasi-static limit. The geothermal convection cells act as natural geobatteries, producing both a telluric electrical current (hence a magnetic field) and an electrical field. Consequently, the measurement of the electrical potential and magnetic field distributions at the surface of a geothermal field should provide an efficient means of monitoring both rate and direction of subsurface fluid flow. We have developed a new set of equations for the material properties entering the macroscopic electrokinetic equations, including the influence of the microstructure, salinity, temperature, and gas and water saturations. However, further investigations are still needed (1) to fully understand the role of pore fluid chemistry on the development of the ζ potential and (2) to extend the present work to fractured porous materials. We believe that the understanding of electromagnetic effects associated with fluid flow and the recording of these effects in a broad frequency range can lead to a strong enhance of our understanding of the dynamics of geothermal systems in natural conditions and/or in production, and volcanic activity forecasting.

Appendix

We report here some useful empirical formulas to estimate the permittivity and electrical conductivity of a NaCl solution as a function of the temperature and salinity. The dielectric constant
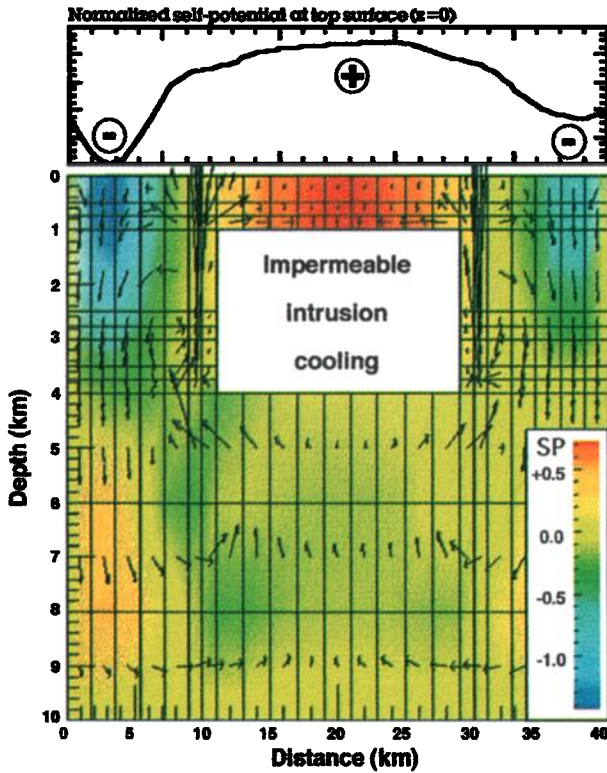
Normalized self-potential at top surface (z=0)

Plate 1. Numerical modeling of the self-potential anomaly associated with the cooling of a dike. The sidewalls and bottom of the structure are closed boundaries for fluid flow and electrical current, whereas the top surface is an open boundary (arrows: Darcy velocity; colors: self-potential distribution).

in the quasi-static limit of a NaCl solution is given as a function of the temperature and salinity by the semi-empirical equations presented by G. R. Olhoeft (1980, unpublished notes)

$$\varepsilon_f(T) = a_0 + a_1 T + a_2 T^2 + a_3 T^3, \quad \text{as } 273 \text{ K} \le T \le 373 \text{ K},\text{(A1)}$$

$$\varepsilon_f(T) = b_0 \frac{1}{T} + b_1 + b_2 T + b_3 T^2 + b_4 T^3, \quad \text{as } 373 \text{ K} \le T \le 643 \text{ K},$$
(A2)

where T is the temperature (in Kelvin), $a_0 = 295.68$, $a_1 = -1.2283$ K^{-1}, $a_2 = 2.094 \cdot 10^{-3}$ K^{-2}, $a_3 = -1.41 \cdot 10^{-6}$ K^{-3}, and $b_0 = 5321$ K; $b_1 = 233.76$, $b_2 = -0.9397$ K^{-1}, $b_3 = 1.417 \cdot 10^{-3}$ K^{-2}, and $b_4 = -8.292 \cdot 10^{-7}$ K^{-3}. The influence of the concentration of NaCl salt is given by G. R. Olhoeft (1980, unpublished notes)

$$\varepsilon_f(C_f;T) = \varepsilon_f(T) + c_1 C_f + c_2 C_f^2 + c_3 C_f^3,$$
(A3)

where C_f is the salt concentration in mol L^{-1}, $c_1 = -13.00$ L mol^{-1}, $c_2 = 1.065$ (L mol^{-1})^2, and $c_3 = -0.03006$ (L mol^{-1})^3. The electrical conductivity of a NaCl solution is given as a function of the temperature and salinity by the semiempirical equation derived by *Sen and Goode* [1992]:

$$\sigma_f(C_f;T) = \left(d_1 + d_2 T + d_3 T^2\right) C_f - \frac{d_4 + d_5 T}{1 + d_6 C_f}\left(C_f\right)^{3/2}.$$
(A4)

where $d_1 = 5.6$, $d_2 = 0.27$, $d_3 = -1.510 \times 10^{-4}$, $d_4 = 2.36$, $d_5 = 0.099$, $d_6 = 0.214$, σ_f is in S m^{-1}, T is in °C, and the salinity in

mol L^{-1}. Equation (A4) can be used over a temperature range of 20°-200°C and over the salinity range 10^{-5}-1 mol L^{-1}.

References

Abdelrahman, E. S. M., and S. M. Sharafeldin, A least-squares approach to depth determination from self-potential anomalies caused by horizontal cylinders and spheres, *Geophysics, 62*, 44-48, 1997.

Anderson, L. A., and G. R. Johnson, Application of the self-potential method to geothermal exploration in Long Valley, California, *J. Geophys. Res., 81*, 1527-1532, 1976.

Antraygues, P., and M. Aubert, Self-potential generated by two-phase flow in a porous medium: experimental study and volcanological applications, *J. Geophys. Res., 98*, 22,273-22,281, 1993.

Apostopoulos, G., I. Louis, and E. Lagios, The self-potential method in the geothermal exploration of Greece, *Geophysics, 62*, 1715-1723, 1997.

Atesok, G., P. Somasundaran, and L. J. Morgan, Charge effects in the adsorption of polyacrylamidees on sodium kaolinite and its flocculation, *Powder Technol., 54*, 77-83, 1988.

Avellaneda, M., and S. Torquato, Rigorous link between fluid permeability, electrical conductivity, and relaxation times for transport in porous media, *Phys. Fluids A, 3*, 2529-2540, 1991.

Avena, M. J., and C. P. De Pauli, Modeling the interfacial properties of an amorphous aluminosilicate dispersed in aqueous NaCl solutions, *Colloids Surf. A, 118*, 75-87, 1996.

Bear, J., *Dynamics of Fluids in Porous Media*, 764 pp., Dover, Mineola, N. Y., 1988.

Bull, H. B., and R. A. Gortner, Electrokinetic potentials, X, The effect of particle size on the potential, *J. Phys. Chem., 36*, 111-119, 1932.

Chandler, R., Transient streaming potential measurements on fluid-saturated porous structures: An experimental verification of Biot's slow wave in the quasi-static limit, *J. Acoust. Soc. Am., 70*, 116-121, 1981.

Chauveteau, G., and A. Zaitoun, Basic rheological behavior of xanthan polysaccharide solutions in porous media: Effect of pore size and polymer concentration, in *Enhanced Oil Recovery*, edited by F. J. Fayers, pp. 197-212, Elsevier, New York, 1981.

Chilindar, G. V., Relationship between porosity, permeability and grain size distribution of sands and sandstones, in *Deltaic and Shallow Marine Deposits*, vol. I, edited by L. M. J. U. Van Straaten, pp. 71-75, Elsevier, New York, 1964.

Clavier, C., G. Coates, and J. Dumanoir, The theoretical and experimental bases for the dual-water model for the interpretation of shaly sands, *Soc. Pet. Eng. J., 24*(2), 153-169, 1984.

Corwin, R. F., and D. B. Hoover, The self-potential method in geothermal exploration, *Geophysics, 44*, 226-245, 1979.

De Groot, S. R., and Mazur, P., *Non-equilibrium Thermodynamics*, North-Holland, Amsterdam, 1962.

Dukhin, S. S., and B. V. Derjaguin, *Surface and Colloid Science*, vol. 7, edited by E. Matijevic, John Wiley, New York, 1974.

Elders, W. A., D. K. Bird, A. E. Williams, and P. Schiffman, Hydrothermal flow regime and magmatic heat source of the Cerro Prieto geothermal system, Baja California, Mexico, *Geothermics, 13*, 27-47, 1983.

Fitterman, D. V., and R. F. Corwin, Inversion of self-potential data from the Cerro-Prieto geothermal field, Mexico, *Geophysics, 47*, 938-945, 1982.

Graciaa, A., G. Morel, P. Saulner, J. Lachaise, and R. S. Schechter, The ζ-potential of gas bubble, *J. Colloid Interface Sci., 172*, 131-136, 1995.

Haartsen, M. W., and S. R. Pride, Electroseismic waves from point sources in layered media, *J. Geophys. Res, 102*, 24,745-24,769, 1997.

Hashimoto, T., and Y. Tanaka, A large self-potential anomaly on Unzen volcano, Shimabara peninsula, Kyushu island, Japan, *Geophys. Res. Lett., 22*, 191-194, 1995.

Hernández, A., F. Martínez, A. Martínez, A. Martín, and Prádanos, Porous structure and surface charge density on the walls of microporous aluma membranes, *J. Colloid Interface Sci., 173*, 284-296, 1995.

Hirasaki, G. J., and J. D. Hellums, A general formulation of the boundary conditions on the vector potential in three-dimensional hydrodynamics, *Q. Appl. Math., 16*, 331-339, 1968.

Holst, P. H., and K. Aziz, Transient three-dimensional natural convection in confined porous media, *Int. J. Heat Mass Tranfer, 15*, 73-90, 1972.

Ishido, T., and H. Mizutani, Experimental and theoretical basis of electrokinetic phenomena in rock-water systems and its applications to geophysics, *J. Geophys. Res., 86*, 1763-1775, 1981.

Ishido, T., H. Mizutani, and K. Baba, Streaming potential using geothermal wells and in situ electrokinetic coupling coefficients under high temperature, *Tectonophysics, 91*, 89-105, 1983.

Ishido, T., T. Kiruchi, N. Matsushima, Y. Yano, S. Nakao, M. Sugihara, T. Tosha, S. Takakura, and Y. Ogawa, Repeated self-potential profiling of Izu-Oshima Volcano, Japan, *J. Geomagn. Geoelectr., 49*, 1267-1278, 1997.

Jarvis, N. L., Effect of various salts on the surface potential of the water-air interface, *J. Geophys. Res., 77*, 5177-5182, 1972.

Jiang, Y. G., F. K. Shan, H. M. Jin, L. W. Zhou, and P. Sheng, A method for measuring electrokinetic coefficients of porous media and its potential application in hydrocarbon exploration, *Geophys. Res. Lett, 25*, 1581-1584, 1998.

Johnson, D. L., T. J. Plona, C. Scala, F. Pasierb, and H. Kojima, Tortuosity and acoustic slow waves, *Phys. Rev. Lett., 49*, 1840-1844, 1982.

Johnson, D. L., T. J. Plona, and H. Kojima, Probing porous media with 1st sound, 2nd sound, 4th sound and 3rd sound, in *Physics and Chemistry of Porous Media*, vol. II, edited by R. Jayanth, J. Banavar, and K. W. Winkler, pp. 243-277, Am. Inst. of Phys., New York, 1986.

Jouniaux, L., and J.-P. Pozzi, Streaming potential and permeability of saturated sandstones under triaxial stress: Consequences for electrotelluric anomalies prior to earthquakes, *J. Geophys. Res., 100*, 10,197-10,209, 1995.

Kawakami, N., and S. Takasugi, SP monitoring during the hydraulic fracturing using the TG-2 well, paper I004 presented at 56th Meeting and Technical Exhibition, Eur. Assoc. of Explor. Geophys., Vienna, Austria, June 6-10, 1994.

Lénat, J.-F., B. Robineau, S. Durand, and P. Bachèlery, A self-potential survey of the summit zone of Khartala volcano (Grande Comore), *C R. Acad. Sci. Paris, 327*, 781-788, 1998.

Lorenz, P. B., Surface conductance and electrokinetic properties of kaolinite beds, *Clays Clay Miner., 17*, 223-231, 1969.

Majaeva, O., Y. Fujinawa, and M. E. Zhitomirsky, Modeling of non-stationary electrokinetic effect in a conductive crust, *J. Geomag. Geoelectr., 49*, 1317-1326, 1997.

Marsden, S. S., Two phase streaming potentials, paper presented at 12th Workshop on Geothermal Reservoir Engineering, Stanford Univ., Stanford, Calif., 1987.

Massenet, F., and V. N. Pham, Experimental and theoretical basis of self-potential phenomena in volcanic areas with reference to results obtained on Mont Etna (Sicily), *Earth Planet. Sci. Lett., 73*, 415-429, 1985.

Mercer, J. W., G. F. Pinder, and I. G. Donalson, A Galerkin-finite element analysis of the hydrothermal system at Wairakei, New-Zealand, *J. Geophys. Res., 80*, 2608-2621, 1975.

Michel, S., and J. Zlotnicki, Self-potential and magnetic surveying of La Fournaise volcano (Réunion Island): Correlations with faulting, fluid circulation, and eruption, *J. Geophys. Res., 103*, 17,845-17,857, 1998.

Morgan, F D., E. R. Williams, and T. R. Madden, Streaming potential of Westerly granite with applications, *J. Geophys. Res , 94*, 12,449-12,461, 1989.

Okada, K., and Y. Akagi, Method and apparatus to measure the ζ-potential of bubbles, *J. Chemical Eng.*, Jpn., *20*, 11-15, 1987.

Olhoeft, G. R., Electrical conductivity, paper presented at Eighth Workshop on Electromagnetic Induction in the Earth and the Moon, Int. Assoc. of Geomagn. and Aeron., Neuchatel, Switzerland, August 1986.

Poirier, J. E., and J. M. Cases, Sur l'origine et la nature de l'interaction adsorbat-adsorbant dans les systèmes à interactions faibles, in *Solid-Liquid Interactions in Porous Media*, 447-462, Ed. Technip, 1985.

Pride, S., Governing equations for the coupled electromagnetics and acoustics of porous media, *Phys. Rev. B, 50*, 15,678-15,696, 1994.

Revil, A., Ionic diffusivity, electrical conductivity, membrane and thermoelectric potentials in colloids and granular porous media: a unified model, *J. Colloid Interf. Sci., 212*, 503-522, 1999.

Revil, A., and L. M. Cathles, Permeability of shaly sands, *Water Resour. Res., 35*, 651-662, 1999.

Revil, A., and P. W. J. Glover, Theory of ionic surface electrical conduction in porous media, *Phys. Rev. B, 55*, 1757-1773, 1997.

Revil, A., and P. W. J. Glover, Nature of surface electrical conductivity in natural sands, sandstones, and clays, *Geophys. Res. Lett., 25*, 691-694, 1998.

Revil, A., and P. A. Pezard, Streaming potential anomalies along faults in geothermal areas, *Geophys. Res. Lett., 25*, 3197-3200, 1998.

Revil, A., L. M Cathles, S. Losh, and J. A. Nunn, Electrical conductivity in shaly sands with geophysical applications, *J. Geophys. Res, 103*, 23,925-23,936, 1998.

Revil, A., P. A. Pezard, and P. W. J. Glover, Streaming potential in porous media, 1, Theory of the zeta potential, *J. Geophys. Res.*, this issue.

Roberts, S. J., J. A. Nunn, L. M. Cathles, and F.-D. Cipriani, Expulsion of abnormally pressured fluids along faults, *J. Geophys. Res., 101*, 28,231-28,252, 1996.

Rutgers, A. J., M. DeSmet, and W. Rigole, Streaming current with non-aqueous solutions, *J. Colloid Interf. Sci., 14*, 330-335, 1959.

Sasai, Y., J. Zlotnicki, Y. Nishida, P. Yvetot, H. Murakami, Y. Tanaka, Y. Ishikawa, S. Koyama, and W. Sekiguchi, Electromagnetic monitoring of Miyake-jima Volcano, Izu-Bonin Arc, Japan: a preliminary report, *J. Geomagn. Geoelectr., 49*, 1293-1316, 1997.

Schwartz, L. M., P. N. Sen, and D. L. Johnson, Influence of rough surfaces on electrolytic conduction in porous media, *Phys. Rev. B., 40*, 2450-2458, 1989.

Sen, P. N., and P. A. Goode, Influence of temperature on electrical conductivity on shaly sands, *Geophysics, 57*, 89-96, 1992.

Sen, P. N., C. Scala, and M. H. Cohen, Self similar model for sedimentary rocks with application to the dielectric constant of fused glass beads, *Geophysics, 46*, 781-795, 1981.

Sill, W. R., Self-potential modeling from primary flows, *Geophysics, 48*, 76-86, 1983.

Sprunt, E. S., T. B. Mercer, and N. F. Djabbarah, Streaming potential from multiphase flow, *Geophysics, 59*, 707-711, 1994.

Turcotte, D., and G. Schubert, *Geodynamics Applications of Continuum Physics to Geological Problems*, 450 pp., John Wiley, New York, 1982.

Waxman, M. H., and L. J. M. Smits, Electrical conductivities in oil-bearing shaly sands, *Soc. Pet. Eng. J., 8*, 107-122, 1968.

Zablocki, C. J., Mapping thermal anomalies on an active volcano by the self-potential method, Kilauea, Hawaii, in *Proceedings of the 2nd U.N. Symposium on the Development and Use of Geothermal Resources*, vol. 2, pp. 1299-1309, U.S. Govt. Print. Off., Washington, D. C., 1976.

Zlonicki, J., and J. L. Le Mouël, Possible electrokinetic origin of large magnetic variations at La Fournaise volcano, *Nature, 343*, 633-635, 1990.

Zlotnicki, J., and J. L. Le Mouël, Volcanomagnetic effects observed on Piton de La Fournaise volcano (Réunion Island): 1985-1987, *J. Geophys. Res., 93*, 9157-9171, 1988.

L.M. Cathles III, and H. Schwaeger, Department of Geological Sciences, Cornell University, Snee Hall, GBRN, Ithaca, NY 14853. (e-mail: cathles@geology.cornell.edu)

P.D. Manhardt, GeoGroup Inc., 130 Forest Home Dr., Suite C, Ithaca, NY, 14850-2746. (e-mail: Manhardt@geogroup-inc.com)

A. Revil, Department of Geophysics, CNRS-CEREGE, BP 80, 13545 Aix-en-Provence, Cedex 4, France. (e-mail: revil@cerege.fr).